General Disclaimer

One or more of the Following Statements may affect this Document

- This document has been reproduced from the best copy furnished by the organizational source. It is being released in the interest of making available as much information as possible.

- This document may contain data, which exceeds the sheet parameters. It was furnished in this condition by the organizational source and is the best copy available.

- This document may contain tone-on-tone or color graphs, charts and/or pictures, which have been reproduced in black and white.

- This document is paginated as submitted by the original source.

- Portions of this document are not fully legible due to the historical nature of some of the material. However, it is the best reproduction available from the original submission.

Produced by the NASA Center for Aerospace Information (CASI)

T-70-50089

LEAS
ity
OL

REPORT NO. GDC-DDB70-009
CONTRACT NAS 8-21465

OCT 1970
RECEIVED
NASA STI FACILITY
INPUT BRANCH

LOW GRAVITY PROPELLANT CONTROL USING CAPILLARY DEVICES IN LARGE SCALE CRYOGENIC VEHICLES

RELATED IRAD STUDIES

FACILITY FORM 602

N71-10764
(ACCESSION NUMBER)

56
(PAGES)

CR-102902
(NASA CR OR TMX OR AD NUMBER)

(THRU)

(CODE)

12
(CATEGORY)

GENERAL DYNAMICS
Convair Division

NOV 1970
RECEIVED
NASA STI FACILITY
INPUT BRANCH

REPORT NO. GDC-DDB70-009

LOW GRAVITY PROPELLANT CONTROL USING CAPILLARY DEVICES IN LARGE SCALE CRYOGENIC VEHICLES

RELATED IRAD STUDIES

August 1970

Prepared Under
Contract NAS8-21465
CONVAIR DIVISION OF GENERAL DYNAMICS
San Diego, California

PRECEDING PAGE BLANK NOT FILMED

FOREWORD

This report summarizes Convair propellant control IRAD studies performed during 1968 and 1969. The Convair propellant management IRAD is directed by R. E. Tatro. Personnel contributing to the work summarized herein were M. H. Blatt, K. R. Burton and E. A. Evans.

PRECEDING PAGE BLANK NOT FILMED

TABLE OF CONTENTS

1 INTRODUCTION 1-1

2 RELATED IRAD STUDIES 2-1

2.1 SCREEN FLOW TESTING 2-1
2.1.1 INTRODUCTION 2-1
2.1.2 SUMMARY 2-1
2.1.3 THEORETICAL BACKGROUND 2-2
2.1.4 EXPERIMENTAL EQUIPMENT AND TECHNIQUES 2-4
2.1.5 INTERPRETATION OF RESULTS 2-9
2.1.6 DUTCH TWILL SCREENS 2-9
2.1.7 CONCLUSIONS AND RECOMMENDATIONS . . . 2-13
2.2 BUBBLE DYNAMICS 2-13
2.2.1 SINGLE BUBBLE DYNAMICS 2-16
2.2.2 BUBBLE ENERGY EQUATION FOR A SINGLE BUBBLE 2-20
2.2.3 WAKE EFFECTS 2-20
2.2.4 AGGLOMERATION AND TANK WALL INTERACTION 2-22
2.2.5 VAPORIZATION 2-23
2.2.6 RECOMMENDATIONS 2-24
2.3 RESIDUAL PROPELLANT PREDICTION 2-25
2.3.1 INTERFACE SHAPE 2-25
2.3.2 FROUDE NUMBER DRAINING (SURFACE TENSION SMALL) 2-25
2.3.3 ZERO-G DRAINING 2-33
2.3.4 RESIDUAL VOLUME PREDICTION 2-38
2.3.5 DRY SCREEN 2-39
2.3.6 INITIALLY WET SCREEN 2-39
2.4 SETTLING ANALYSIS 2-40
2.5 SURFACE TENSION PROPERTY VALUES . . . 2-40

3 REFERENCES 3-1

PRECEDING PAGE BLANK NOT FILMED

ILLUSTRATIONS

Figure		Page
2-1	Schematic of Test Tank and Plumbing	2-5
2-2	Schematic of Test Setup	2-6
2-3	Cryogenic Flow Test Section	2-7
2-4	Schematic of Test Section	2-8
2-5	Reynolds Number Effects on Dimensionless Pressure Drop (Po) for Dutch Twill Screens	2-10
2-6	Low Reynolds Data Compared with Capillary Screen Flow Model	2-11
2-7	Screen Flow Data Using Armour and Cannon Geometry	2-12
2-8	Neniscus Volume for a Liquid with Contact Angle Zero in a Right Circular Cylinder	2-26
2-9	Open Channel Model Nomenclature	2-28
2-10	Comparison of Suction Dip Correlations	2-29
2-11	Pullthrough with Baffled Drain	2-30
2-12	Pullthrough with a Sump and Baffled Drain	2-31
2-13	Pullthrough with Sump and Screen Over Drain	2-32
2-14	Low-G Baffled Draining	2-35
2-15	Film Thickness Vs Interface Distortion Parameter	2-37
2-16	Schematic of Start Basket Draining	2-38
2-17	Surface Tension of Liquid Hydrogen	2-41
2-18	Surface Tension of Liquid Oxygen	2-42
2-19	Surface Tension of Liquid Fluorine	2-43
2-20	Surface Tension of Liquid Nitrogen	2-44
2-21	Surface Tension of Helium	2-45

TABLES

2-1	Summary of Screen Flow Tests	2-4
2-2	Screen Geometry, Flow and Wicking Data, Dutch Twill Screens	2-14
2-3	Screen Geometry, Square Weave Screens	2-14

PRECEDING PAGE BLANK-NOT FILMED.

SUMMARY

This report contains studies performed under the Convair 1968 and 1969 Cryogenic Propellant Management IRAD which are closely related to the subject matter of Contract NAS8-21465. Studies summarized herein include screen flow testing, bubble dynamics, pullthrough and residual prediction, settling, and a survey of surface tension property values.

Dutch twill and square weave screens were tested to determine pressure drop characteristics in both the laminar and turbulent regimes using liquid and gaseous hydrogen and nitrogen, water and gaseous helium. Data for the dutch twill screens was then correlated by means of a semiempirical expression containing both viscous and inertial terms. Square weave screen data agreed with an existing correlation based on a sudden expansion model.

Analytical expressions were derived for low gravity and normal gravity pull through which can be used for both baffled and unbaffled tanks. These relationships, when combined with the flow equations of a capillary device in a draining tank and screen flow data, yield a set of simultaneous differential equations which when solved numerically provide a useful tool for predicting propellant residuals.

An analytical model was developed to describe the temporal and spatial evolution of bubbles in low gravity environments. A knowledge of bubble phenomena is significant in the design of many items of space hardware. The analytical model considers interactions between neighboring bubbles. Populations are limited to 1000 bubbles existing from 100 possible sites. The model has been programmed and sample cases are discussed which show the importance of agglomeration in low-g. A comparison illustrates the effects of wake interactions. Energy transport between the bubble and the liquid phase is considered during its transit. Two methods of bubble generation and growth are considered, nucleate boiling and bulk boiling due to saturation temperature change.

A simplified Marker and Cell (SLOSH) computer code was checked out by running a settling problem related to the S-IVC. The code was not able to predict violent recirculation and turbulence subsequent to fluid impact on the aft bulkhead.

An extensive survey of the literature was performed to obtain accurate property values for surface tension and contact angle, and reliable values for design are recommended. Surface tension vs temperature curves are plotted for LH_2, LO_2, LN_2, LH_2 and LHe. Contact angle for these fluids was found to be zero for all known surfaces.

1

INTRODUCTION

Convair's Cryogenic Propellant Management has been a continuing program dating back more than seven years involving the thermodynamics and fluid mechanics of orbital cryogenic propellant behavior. Studies which had been performed prior to the initiation of NAS8-21465 in the past included programs in the areas of low g propellant and venting, scaling, low-g thermodynamics and stratification. These studies formed a base of knowledge which was utilized in this contract. During the course of Contract NAS8-21465 IRAD studies were performed to develop basic knowledge in the areas of screen flow testing, vapor pullthrough, residual prediction, settling, and low-g bubble dynamics and to survey available information on cryogenic surface tension properties. These programs were general in nature and not devoted to studying specific contract problems however, the information developed was in a form which was readily utilized in performing contract tasks. As an example, basic screen flow data and pullthrough correlations were taken from IRAD results and formulated into outflow computer programs to analyze specific contract mission conditions for the S-IVC vehicle. The IRAD studies which are summarized in this report were previously presented in References 1 and 2. Related IRAD studies are presented in this document to fulfill requirements of Contract NAS8-21465, Article XII.

"It is mutually agreed and understood that the Contractor's Independent Research and Development (IRAD) program includes certain studies and investigations closely related to the subject matter of this contract. The Contractor agrees to make the results of this supporting and supplemental effort available to the Government as they become available, and in any event by inclusion in the Final Report to be furnished under this contract. This agreement by the contractor shall not preclude the Contractor's right to recover the costs of performing such work as part of his IRAD program under his approved system of accounting,"

2

RELATED IRAD STUDIES

The following sections present work performed under Convair IRAD programs in technical areas which are directly related to Contract NAS8-21465. The information condensed presented is in the areas of screen flow testing, bubble motion, residual analysis, settling, and surface tension properties. For a more complete treatment of these topics, see References 1 and 2.

2.1 SCREEN FLOW TESTING

2.1.1 INTRODUCTION–Convair screen flow testing was conducted in consecutive IRAD programs in 1968 and 1969. Tests in 1968, with cryogenic fluids in a triple walled dewar, indicated the feasibility of predicting cryogenic screen flow pressure drop with non-cryogenic fluids. Results of the 1969 program were semiempirical equations for predicting screen flow in square weave and dutch twill screens. A complete presentation of the two programs, briefly described below, is given in References 1 and 2.

2.1.2 SUMMARY–Knowledge of screen flow characteristics is essential for design of surface tension systems for propellant control and transfer applications. This information is required for predicting residuals during tank draining, vapor ingestion during restart, wicking and system refilling.

Reliable correlations for determining screen flow pressure drop for cryogenic fluids have not been reported in the literature. The sparse data reported for dutch twill screens with non-cryogenics has been in the low Reynolds regime only. Due to the lack of data and uncertainty as to the validity of the information which is available, an experimental program was initiated in order to provide useful screen correlations over the range of Reynolds numbers required for practical surface tension system design.

Testing was initially conducted primarily with cryogenic fluids for three dutch twill screens and one square weave screen using a vacuum jacketed, liquid jacketed dewar. Instrumentation accuracy, for the low pressure drops measured, was assured by submerging the cryogenics in the test dewar.

After test results proved the flow similarity between cryogenic and non-cryogenic test fluids, six additional dutch twill screens were tested with GH_2 and GN_2 to obtain sufficient data to attempt to correlate analytical and semiempirical models.

Two theoretical models were investigated in detail; a capillary model based on the Hagen-Poiseuille Equation for fully developed laminar flow and a semi-empirical model suggested by Armour and Cannon (Ref. 3) which visualized the screens as a collection of submerged objects for laminar flow and as a bundle of tubes of diameter D for turbulent flow. Neither model was adequate in predicting the accurate screen flow data obtained in the current investigation. The most effective method of representing the test data is in the form of empirically obtained viscous and inertial dimensionless coefficients shown in Table 2-2 and defined by Equation 2-2.

2.1.3 THEORETICAL BACKGROUND — At low Reynolds numbers the flow through a porous medium can be modeled by straight parallel capillaries of uniform diameter. Flow and pressure loss in one capillary are related by the Hagen-Poiseuille equation for fully developed laminar flow:

$$Q = - \frac{D^2 A \Delta P}{32 \mu L} \qquad (2\text{-}1)$$

where Q is the volume flow rate, D is the capillary diameter, A is the flow area, μ is the dynamic viscosity of the fluid and $\Delta P/L$ is the pressure gradient in the direction of flow.

The major problem involved in utilizing Equation(2-1)for screen flow is determining the representative capillary diameter and free flow area to be used. Mercury intrusion techniques can be used to determine the average capillary diameter and porosity which appear to be useful for this purpose, Ref. 4 . This procedure involves measuring the volume of mercury which is being forced into a porous material with steadily increasing pressure. Forces resisting intrusion of mercury into the material depend only on the surface tension of the mercury and the diameter of the pores being filled. Reference 1 shows that the average capillary diameter can be found from

$$D_a = \frac{1}{V_o} \sum_{D=0}^{\infty} D \, \Delta V$$

and the porosity can be found as

$$\phi = \frac{V_o}{V_o + V_s}$$

where D is the capillary diameter, ΔV is the incremental volume penetrated between successively smaller pore sizes, V_o is the total void or pore volume of the sample, and V_s is the solid volume of the sample.

Armour and Cannon. Reference 3, correlated pressure drop-flow data with a semi-empirical model. Their experimental program consisted of flowing helium and nitrogen through square, fourdrinier and dutch weave screens using rotometers to measure the pressure drop across the screen sample. The experimental results were used to obtain the coefficients α and β in the following equation

$$f = \frac{\alpha}{Re} + \beta$$

Re = Reynolds number

where

$$f = \frac{\Delta P \, g_c \, \epsilon^2 \, D}{Z \, B \, \rho \, V^2}$$

ϵ = porosity

Z = tortuosity

B = screen thickness

D = screen bubble point

$$N_{Re} = \frac{\rho \, V}{\mu \, a^2 \, D}$$

a = surface volume ratio

The viscous resistance coefficient is α and β is the inertial resistance coefficient. The arrangement of a, ϵ and D was made to expediently fit the data. D, the bubble point of the screen, is only coincidentally a flow geometry property if bubble point is proportional to the average capillary diameter. (The bubble point is a measure of the largest pore in the screen).

Square weave screen flow models for high Reynolds number flow originate predominately from a one dimensional incompressible stream with a sudden expansion. Assuming potential flow at the inlet and balancing momentum loss with pressure recovery in the turbulent jet behind the screen one arrives at the expression $Eu = [S/(1-S)]^2$, where $S = 1-\phi$, for round wire screens, Reference 5, and ϕ is the porosity.

Several investigators have examined the region between the viscous regime governed by Darcy's law and the inertial regime characterized by a constant Euler number. Equations have been postulated with both viscous and inertial terms which are designed to cover the full range of Reynolds number. Expressions of this type have not been adequately correlated with experimental data. The transition between viscous and inertia dominated flow is difficult to predict without experimental data. Transition should be a function of the Reynolds number for a particular porous material, however, the value of the Reynolds number apparently depends upon pore size distribution and capillary curvature which cannot be evaluated without testing. Once the transition Reynolds number is determined for a particular porous material and fluid, however, this Reynolds number should hold for other fluids with the same material.

2.1.4 EXPERIMENTAL EQUIPMENT AND TECHNIQUES — Tests were run on 200 × 600, 165 × 1400, 200 × 1400 and 20 × 20 mesh screens in the cryogenic test setup shown schematically in Figure 2-1. Noncryogenic tests with GH_2 and GN_2 were run for 165 × 800, 80 × 700, 50 × 250, 30 × 250, 20 × 250 and 80 × 700 screens in the test setup shown in Figure 2-2. A summary of the tests run is given in Table 2-1.

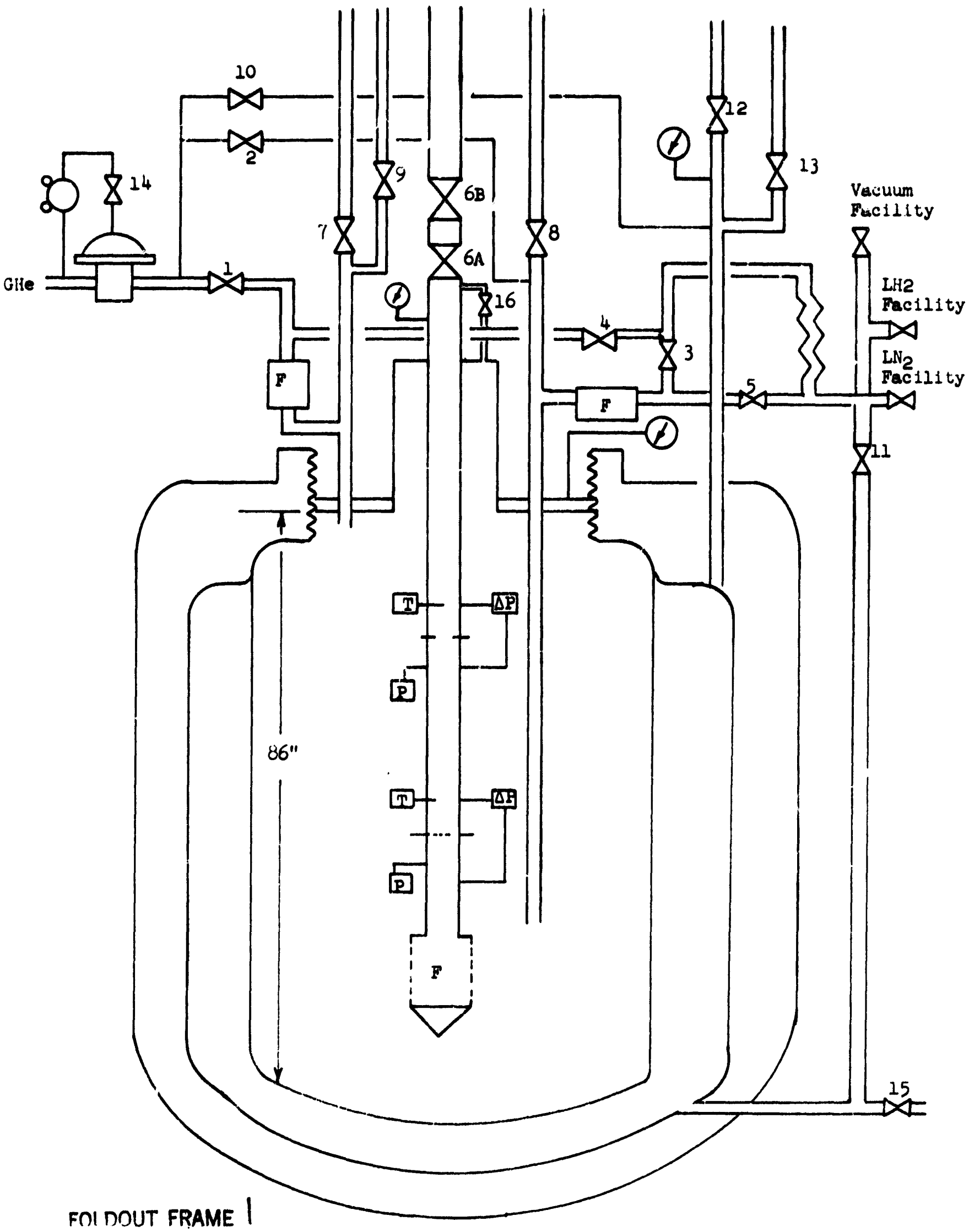
For the cryogenic tests, screens were mounted into a test section as shown schematically in Figure 2-3. The filter upstream of the screen straightened the flow and removed impurities from the test fluids, and the orifice downstream was used to measure the flow rate. Pressure drops were measured using transducers submerged and calibrated in the test fluid for maximum accuracy. Platinum resistance probes were used to measure temperatures. The test section was mounted in the test tank shown schematically in Figure 2-1. This tank has both a vacuum and liquid jacket, thus combining easy access through the manhole cover at the top of the tank with a low heat flux environment in the bottom of the tank. The tank was pressurized to maintain cryogenics in the test section in a subcooled state assuring single phase fluid flow through the screen. All cryogenic tests were run within this test tank while helium and water tests with the first four samples, were run outside the tank using the test section with modified set ups.

The 1969 noncryogenic tests were run using the test section and setup shown in Figures 2-2 and 2-4. Instrumentation was similar to the tests run in 1968. The vaporizing coil was used to convert LH_2 and LN_2 to a gas and the conditioning coil had sufficient thermal inertia to eliminate any rapid temperature fluctuations. The orifice used with each specimen was sized to give an orifice and screen ΔP which were equal at .7 psid using GN_2 at ambient temperature. Some tests were run as low as -260°F at the maximum pressure differential in order to obtain high Reynolds number data.

Table 2-1 . Summary of Screen Flow Tests

Screen Mesh (No. of Wires per Inch)	Type of Weave	Fluids Tested
200 × 1400*	Dutch Twill	GHe, LH_2, GH_2, LN_2, GN_2, Tap Water, Distilled Water
165 × 1400*	Dutch Twill	GHe, LH_2, GH_2, LN_2, GN_2
200 × 600*	Dutch Twill	GHe, LH_2, GH_2, LN_2, GN_2
20 × 20	Square	GHe, LH_2, GH_2, LN_2, GN_2, Tap Water
80 × 700	Dutch Twill	GH_2, GN_2
165 × 800	Dutch Twill	GH_2, GN_2
150 × 700	Dutch Twill	GH_2, GN_2
30 × 250	Dutch Twill	GH_2, GN_2
50 × 250	Dutch Twill	GH_2, GN_2
20 × 250	Dutch Twill	GH_2, GN_2

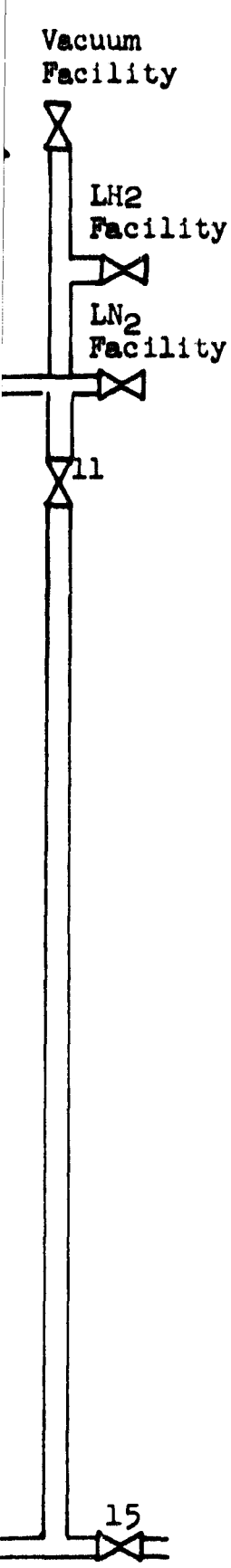
* 1968 Testing



1. 1
2. 2
3. 3
4. 4
5. 5
6a. 6A
6b. 6B
7. 7
8. 8
9. 9
10. 10
11. 11
12. 12
13. 13
14. 14
15. 15
16. 16
ΔP ΔP
P P
T T
F F

FOLDOUT FRAME 1

Figure 2-1. Schematic of Test Tank and Plumbing



1. GHe inlet, inner tank top - 1" ball valve
2. GHe inlet, inner tank bottom - 1/2" globe valve
3. GH_2/GN_2 inlet, inner tank bottom - 1" ball valve
4. GH_2/GN_2 inlet, inner tank top - 1" ball valve
5. LH_2/LN_2 fill, inner tank - 1" globe valve

6a. Test section vent - 2" or 1/2" gate (throttling)

6b. Test section vent backup - 2" globe with remote actuator

7. Inner tank vent - 2" globe valve
8. Inner tank drain - 1" ball valve
9. Inner tank relief - 1" 100 psi set
10. GHe inlet, guard tank - 1/2" globe valve
11. LH_2/LN_2 fill, guard tank - 1" ball valve
12. Guard tank vent - 3" gate valve
13. Guard tank relief - 3" 10 psi set
14. Regulator dome shutoff - 1/4" globe valve
15. Guard tank drain - 1" ball valve
16. Test section bypass - 1/2" ball valve

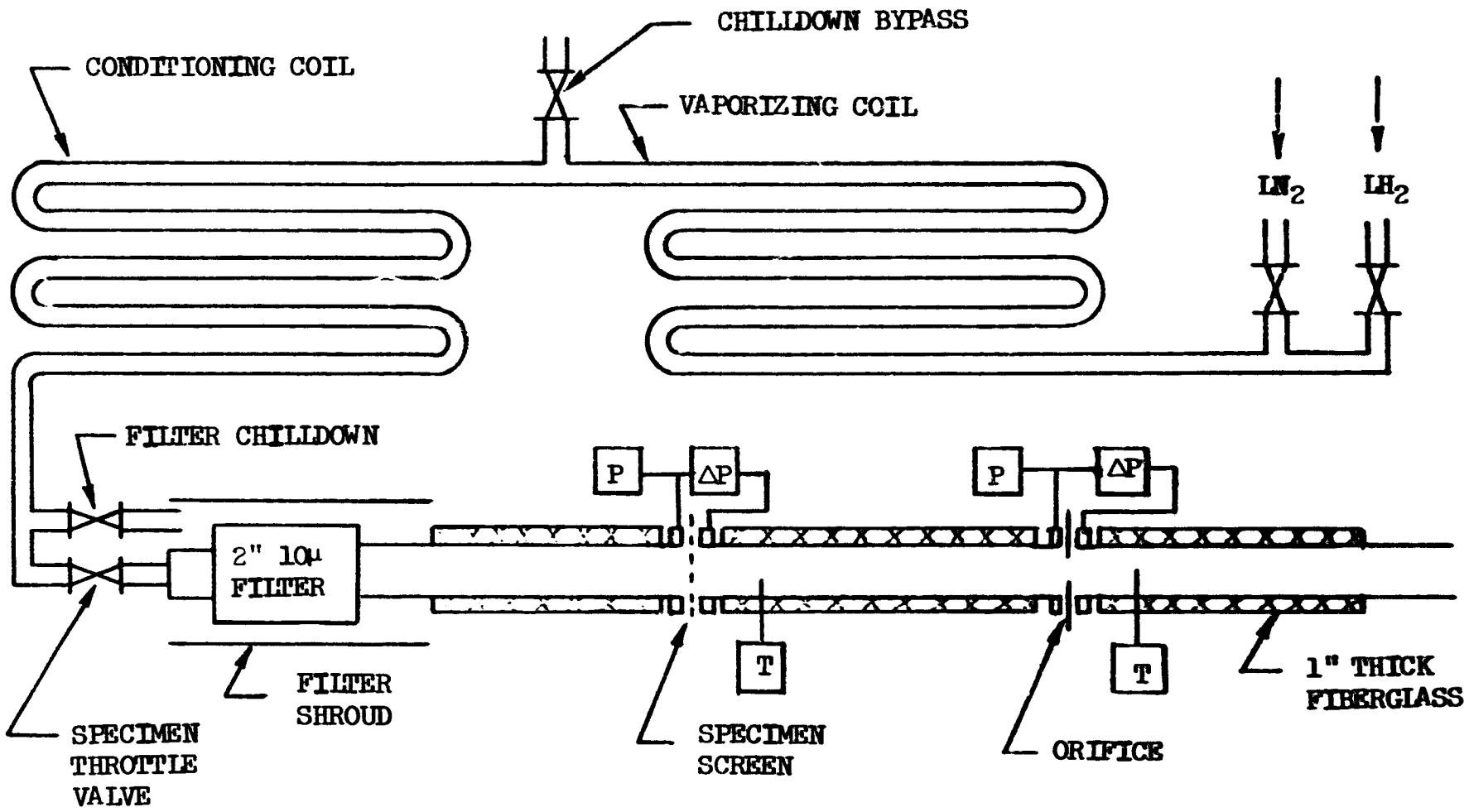
ΔP - Differential pressure transducer

P - Absolute Pressure Transducer

T - Temperature Transducer

F - Filter

FOLDOUT FRAME 2



P	0 TO 100 PSIA STATHAM FULL BRIDGE PRESSURE TRANS.
ΔP	0 TO 0.7 PSID STATHAM FULL BRIDGE PRESSURE TRANS.
T	+ 100°F TO -430°F ROSEMONT PLATINUM TEMPERATURE PROBES

Figure 2-2. Schematic of Test Setup

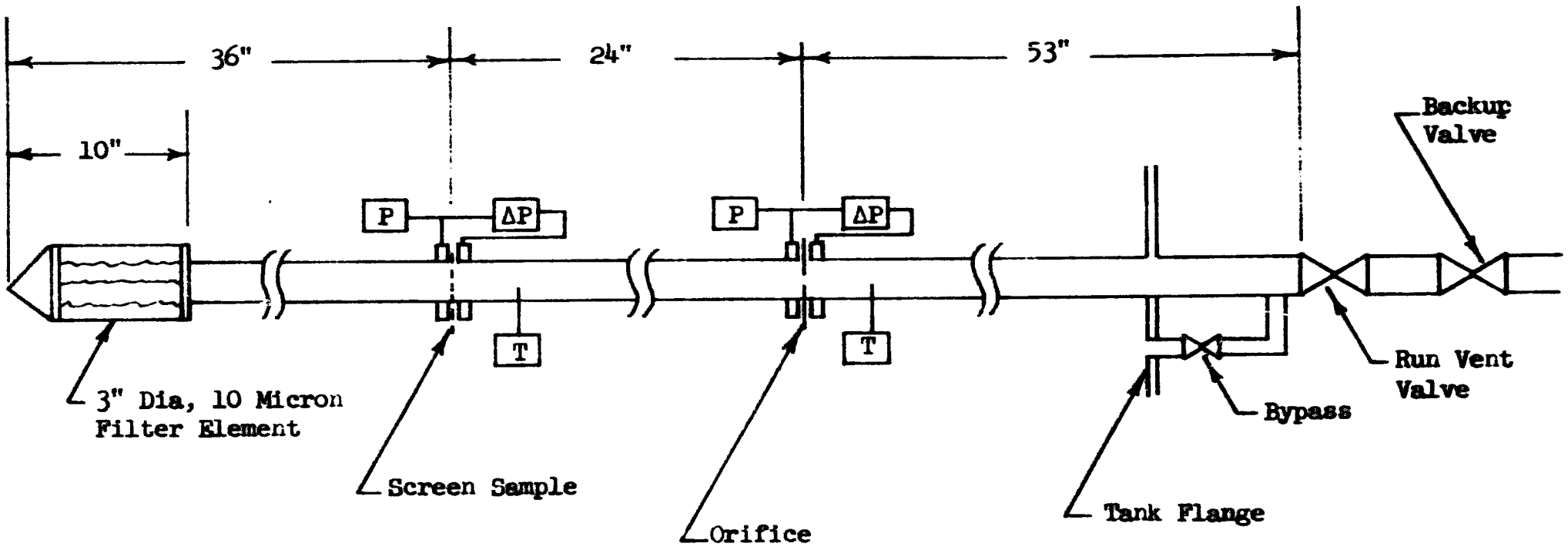


Figure 2-3. Cryogenic Flow Test Section

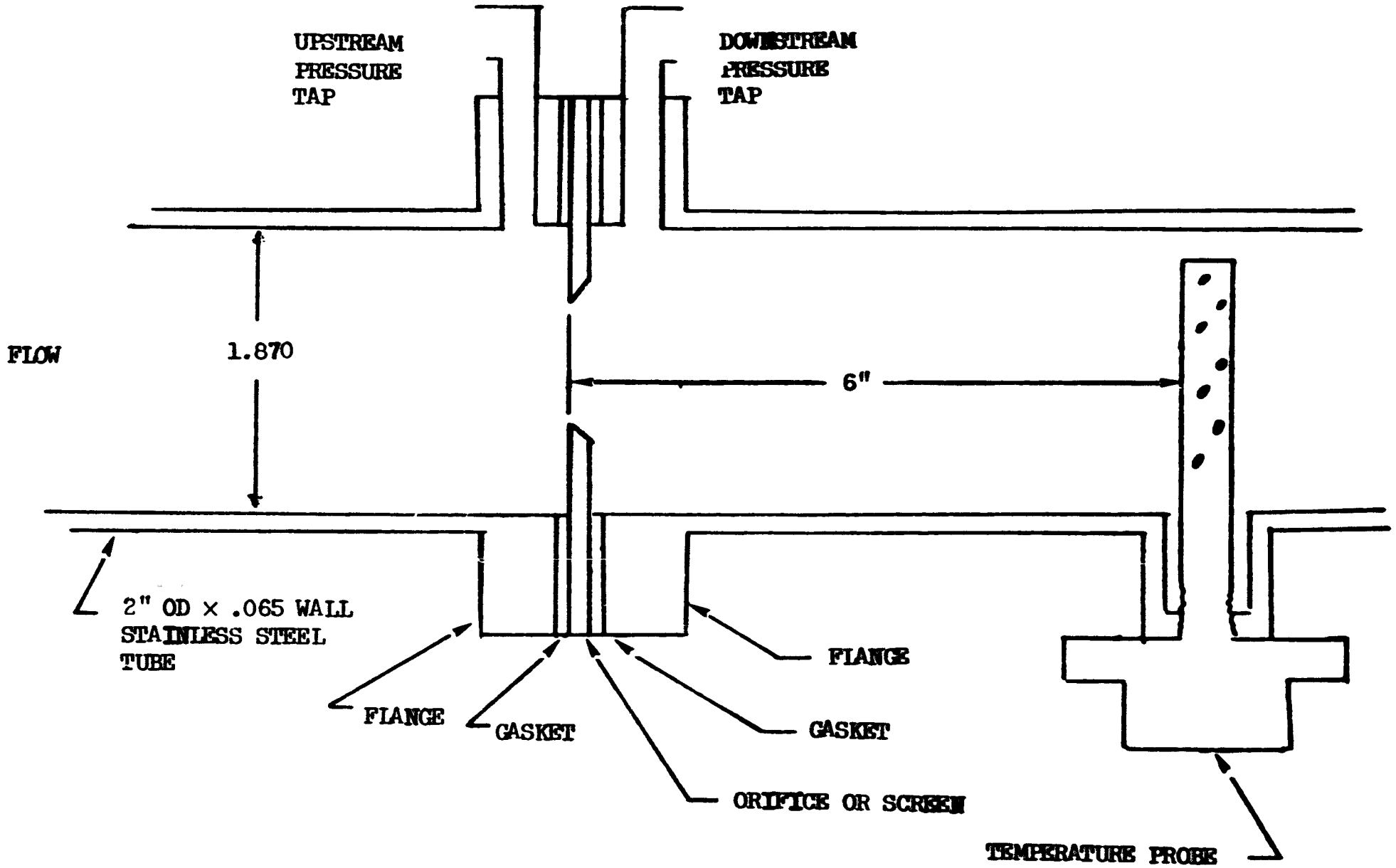


Figure 2-4. Schematic of Test Section

2.1.5 INTERPRETATION OF RESULTS — Test data was reduced by a digital computer program written specifically for this purpose. Mass flow rates through the screens were computed accurately by providing a table of orifice flow coefficients and iterating through a double interpolation routine. Calibration factors were allowed to vary with temperature by tabular interpolation to provide maximum accuracy for those runs at a temperature between calibration points.

Screen data was correlated in two regimes. At very low Reynolds numbers viscous shear in the fluid adjacent to the solid screen surface contributes greatest to the pressure losses, and the Poiseuille number ($Po = \Delta P\ D_a/\mu\ u_o$) is the important parameter. At high Reynolds numbers the Euler number ($Eu = \Delta P/\rho u_o^2$) is the important parameter, a fact that is derivable from the form of the energy dissipation in fully developed turbulence: $\epsilon \sim (\Delta u)^3/\ell$.

Euler number and Poiseuille number were plotted against Reynolds number for each screen. Data for the Dutch Twill screens shown in Figure 2-5 is representative of these plots. Data groupings clearly illustrate that flow similarity exists for cryogenic and noncryogenic fluids in a given screen. It should be noted that no significant variation was observed with Mach number which indicates that all results can be considered representative of incompressible flow. The data clearly shows the Reynolds numbers at which the flow departs from the limiting cases discussed previously. The practical Reynolds number limits ($Re_D \equiv \rho u_o\ D_a/\mu$) obtained from this test program are;

Viscous Regime, Hagen Poiseuille Law, $Re_{D_a} < 1$
Inertial Regime, Turbulent Energy Dissipation, $Re_{D_a} > 100$

2.1.6 DUTCH TWILL SCREENS. For the low Reynolds regime the Hagen Poiseuille model was completely inadequate in predicting pressure drop as illustrated by Figure 2-6. Dutch twill data was also compared with the Armour and Cannon correlation, Reference 3, using bubble point data and calculated porosity, surface to volume ratio and screen thickness. Another comparison was made using average capillary diameter, measured screen thickness and calculated surface to volume ratio. Surprisingly, less scatter was found when comparing data using bubble point diameter than with average capillary diameter. The data for the six screens tested in 1969 was combined with the data from the three screens tested in 1968 in Figure 2-7, in order to develop a single correlation using Armour and Cannon parameters. This single equation is $f = (2.49/Re) + .3$, which compares to $f = 8.61/Re) + 0.52$ found by Armour and Cannon, where $f = (\Delta P g_c \epsilon^2\ D)/(L\rho\mu^2)$ and $Re = (\rho V)/[\rho\mu\ (a^2 D)]$ as indicated in Reference 3, p. 3-18. Examining Figure 2-7 indicates that considerable error could arise in attempting to represent the data by a single correlation, inspite of the convenience of this single correlation.

The most accurate approach is to represent the data for each screen by a single equation of the form $Eu = [A\ (\phi)/Re\ ] + B(S)$ where Eu is the Euler No. $= (2g_c\ \Delta P)/\rho V^2$,

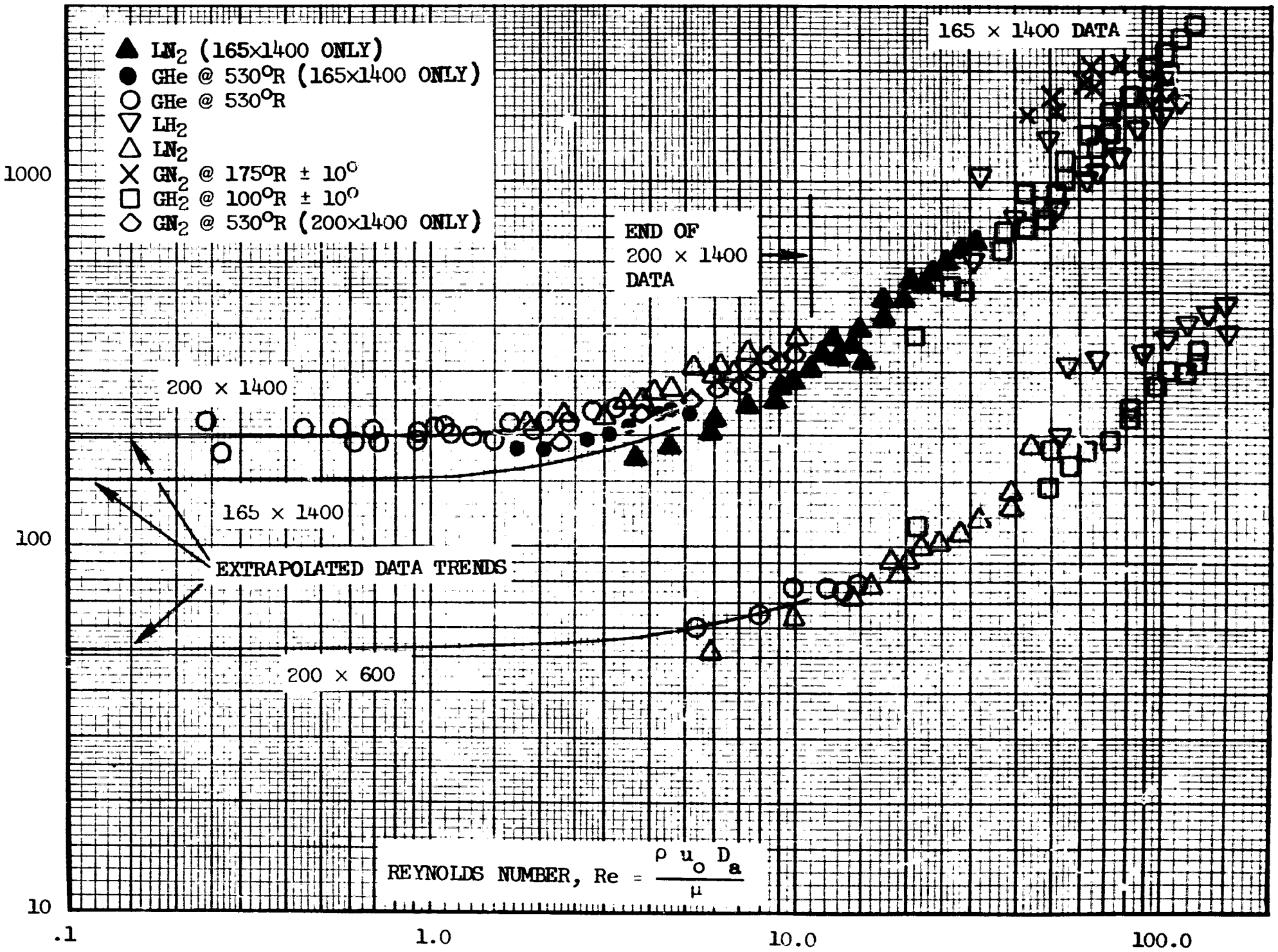


Figure 2-5. Reynolds Number Effects on Dimensionless Pressure Drop (Po) For Dutch Twill Screens

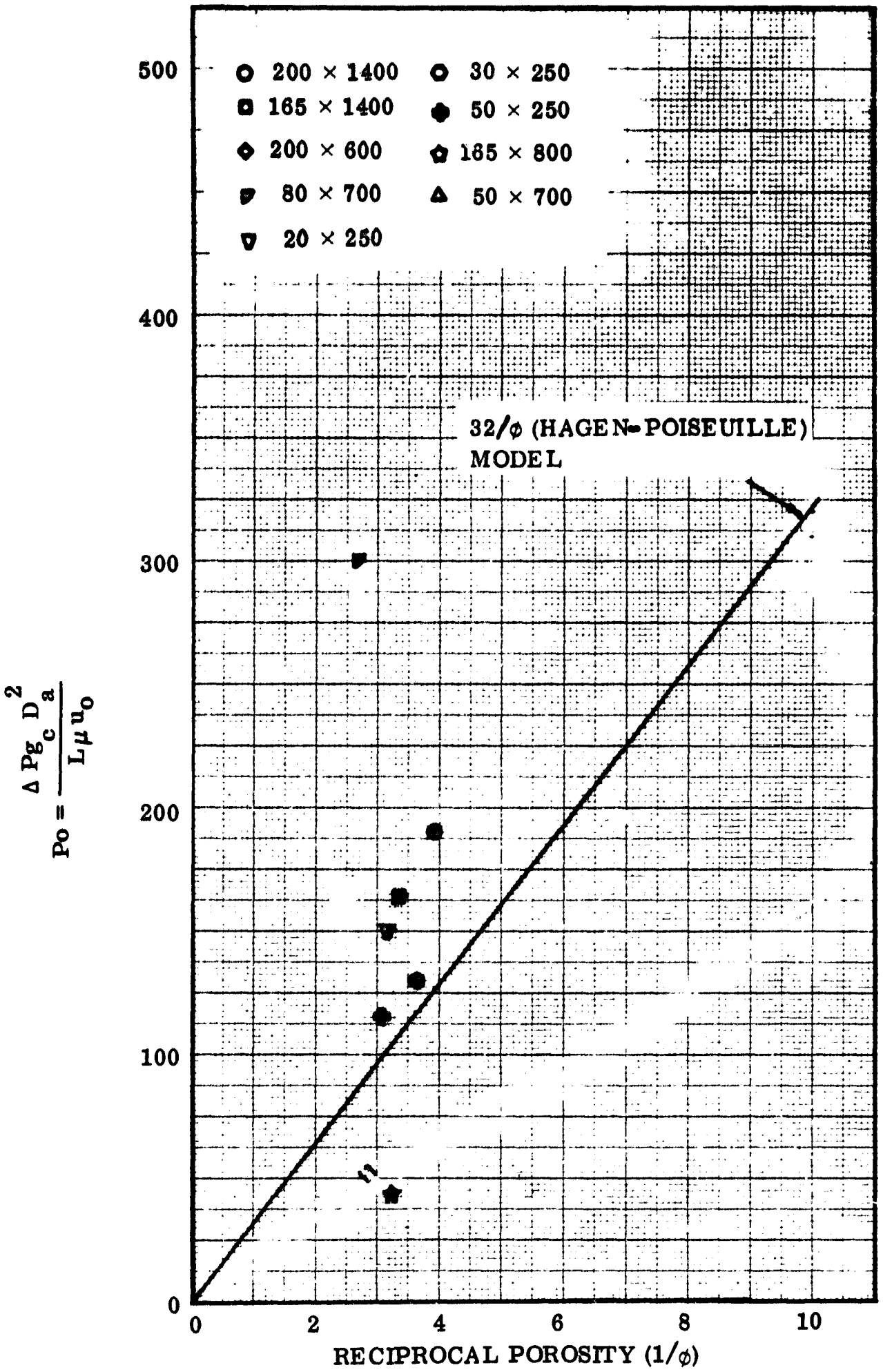


Figure 2-6. Low Reynolds Data Compared With Capillary Screen Flow Model

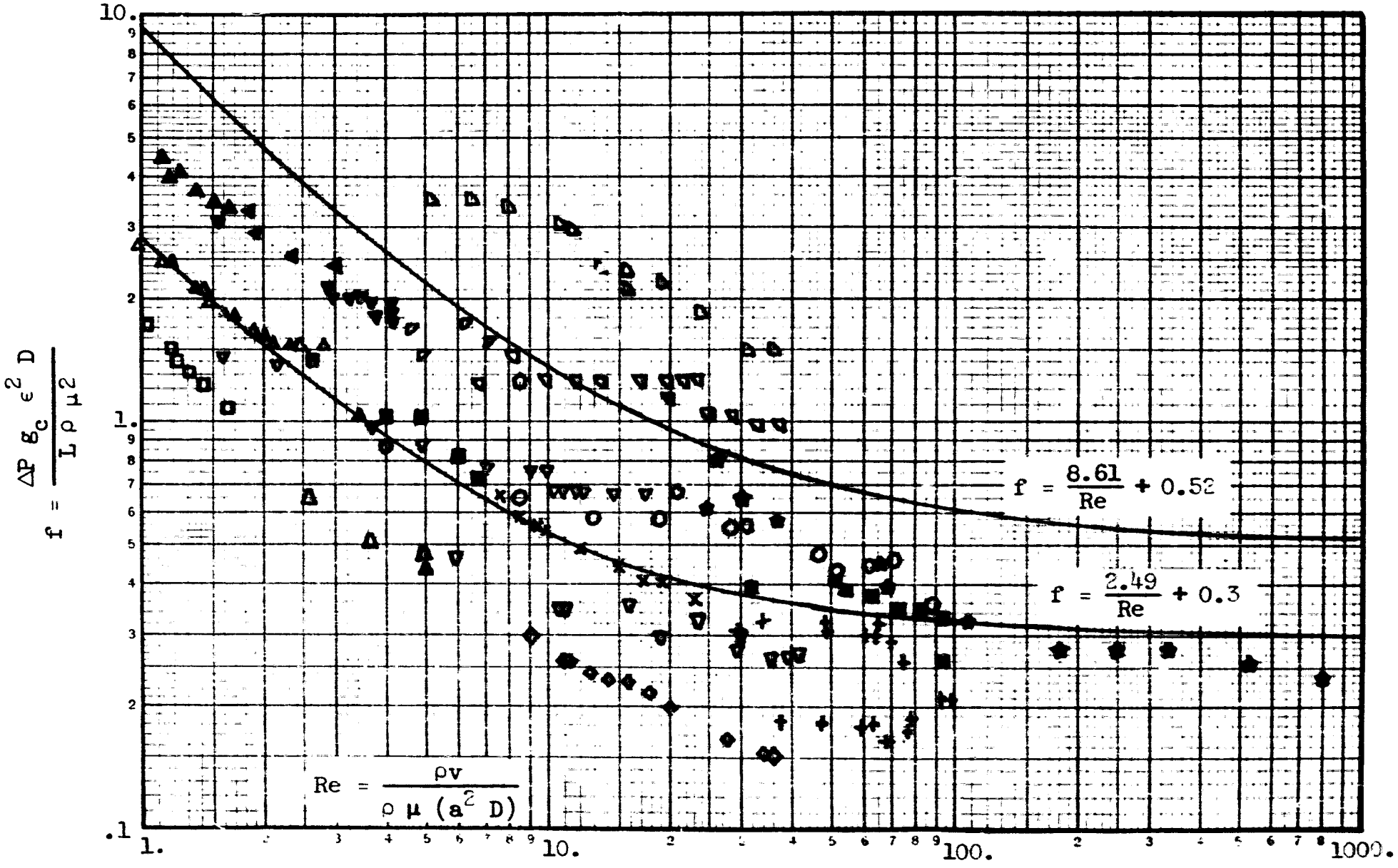


Figure 2-7. Screen Flow Data Using Armour and Cannon Geometry

Re is the Reynolds No. = $(\rho V D_{wire})/\mu$ and A(ϕ) and B(S) are constants for each screen. Rearranging terms in the manner of Reference 3 , p. 2-51, we can write an equation in the form of

$$\Delta P = \frac{A_1 L}{D_a^2 g_c} \mu V + \frac{A_2 L}{D_a g_c} \rho V^2 \qquad (2\text{-}2)$$

where L is the screen thickness, D_a the average capillary diameter, μ the fluid viscosity, ρ the fluid density, V the free stream velocity upstream of the screen, A_1 the viscous constant and A_2 the inertial constant. A_1 and A_2 are found by examining the test data in the low Reynolds number regime and high Reynolds number regime respectively. This procedure is illustrated in Figures 2-27 and 2-28 of Reference 3. The constants A_1 and A_2 are tabulated in Table 2-2 for each of the screens tested. Average capillary diameter for the six screens tested in 1969 was found using macroporosimeter results. Comparing pore volume from microporosimeter to macroporosimeter volumes indicates that the macroporosimeter covers the complete pore spectra for the six screens tested in 1969 while the microporosimeter covers the complete pore volume for the screens measured in 1968. It was not necessary, therefore, to use geometry data based on combining macroporosimeter and microporosimeter test results.

Square weave screen data for the 20 × 20 mesh screen agreed with the equation $Eu = (S/1\text{-}S)^2$.

2.1.7 CONCLUSIONS AND RECOMMENDATIONS — The theoretical and semiempirical models presented were not adequate to represent dutch twill data. The inertial and viscous coefficients obtained experimentally and shown in Table 2-2 are recommended for determining accurate pressure drops for the nine screens tested. These nine screens should include any dutch twill screen which would be considered for a capillary device design.

The correlation shown above is recommended for use in determining pressure drops for square weave screens.

The information presented may be applied directly to spilling, vapor ingestion, residual and refilling calculations and has in fact been incorporated in the DREGS2 and INGASP computer programs.

2.2 BUBBLE DYNAMICS

The position of vapor in the tank may be important in determining heat transfer into the fluid within the start basket. Also vapor positioning by means of geometry may be helpful in control of the liquid vapor interface under the influence of adverse buoyancy

Table 2-2. Screen Geometry, Flow and Wicking Data, Dutch Twill Screens

Screen Mesh	D_B Bubble Pt. Diameter (Microns)	D_A Avg. Capillary Dia. (Microns)	L Thickness (in.)	Porosity (Meas.)	Dimensionless A_1	Dimensionless A_2	Dimensionless Wicking A_W	$A=\frac{A_1 L}{D_a^2 g_c}$	$B=\frac{A_2 L}{D_a g_c}$
200 × 1400	13.4	22.8*	0.0058	0.256	190	18		509687	3.61
165 × 1400	18.6	28.3*	0.0060	0.301	150	16	580	270185	2.68
200 × 600	19.05	36.7*	0.0055	0.347	52	3	368	51053	0.355
165 × 800	22.7	48.5**	0.0065	0.310	43	135		28568	14.3
150 × 700	22.7	60.8**	0.0070	0.171	500	133		227642	12.08
80 × 700	29.7	139.3**	0.0098	0.416	1000	34	6230	121427	1.89
50 × 250	33.9	129.5**	0.0127	0.325	115	191		20938	14.78
30 × 250	48.5	112.2**	0.0265	0.276	130	12	1120	65795	2.23
20 × 250	52.8	155.3**	0.0280	0.325	150	20		41869	2.84

*Microporosimeter
**Macroporosimeter

Table 2-3. Screen Geometry, Square Weave Screens

Mesh	(Microns) D_B	Solidity S
400 × 400	38	0.64
325 × 325	44	0.44
200 × 200	74	0.66
150 × 150	104	0.63
100 × 100	140	0.698
80 × 80	180	0.686
50 × 50	280	0.700
40 × 40	440	0.640
20 × 20	860	0.538

and thermophoretic forces. For these reasons a program was developed to predict bubble dynamics in low gravity environments.

In order to evaluate thermodynamic and kinematic properties of the propellant in a low gravity environment, knowledge of heat transfer to the stored contents, the moments of inertia, and liquid location are required.

Heat transfer to the propellant is defined by the liquid level, its orientation, and energy transport mechanisms at the tank wall. The latter necessitates a specification of boiling parameters, e.g. number of sites, radius of each site, and frequency of production at each site.

The propellant moments of inertia and the liquid location are determined by the spatial distribution of voids, heat transfer and void generation, surface orientation, and pressure transient of the tank contents. Additional requirements for void distribution specification are generated by propellant venting and outflow problems, e.g. vapor entrainment.

An investigation and computer program development has been undertaken to provide the prediction and pre-design definition of the previously mentioned variables. The resulting computer program (EVOLVE) describes the temporal and spatial evolution of a bubble society. The phenomenological considerations which are embodied in the program are:

1. Bubble generation with time and spatial dependent radii and frequencies.

2. Kinematics and energetics of a single bubble moving in temperature and inertial acceleration fields in three dimensions.

3. Time and spatial dependent temperature and inertial acceleration fields.

4. The effect of wake behind a bubble on following bubbles.

5. Bubble agglomeration (collision absorption).

6. Slip or no-slip interaction with tank walls.

7. Interaction of a single bubble with porous walls (screens).

8. Vaporization (2 ways).

   a. Nucleate boiling as mentioned.

   b. "Bulk" boiling due to change in state of liquid (pressure decay) - this vapor generation is partitioned between the liquid-ullage interface and the existing bubble population in proportion to relative surface areas.

9. Liquid energy conservation, outflow, and level determination.

10. Convective heat transfer to liquid phase which is dependent on liquid level.

The program is designed to consider populations of up to 1,000 bubbles, three dimensional transport, bubble dependent surface orientation (not necessarily normal to inertial acceleration vector), and time dependent ullage pressure history. Analytical treatments of the above phenomena which are incorporated in the program are described in the following sections.

2.2.1 SINGLE BUBBLE DYNAMICS — The motion of a bubble moving in a liquid with noncolinear gravitational and temperature fields is considered by summing the body and surface forces acting on the bubble, neglecting the bubble inertia.

$$\vec{F}^{B} + \vec{F}^{ST} + \vec{F}^{D} = 0 \qquad (2\text{-}3)$$

$\vec{F}^{B}$ ≡ buoyant force

$\vec{F}^{ST}$ ≡ surface tension force resulting from liquid temperature gradient

$\vec{F}^{D}$ ≡ liquid-bubble momentum exchange (drag)

The equation of motion for a bubble, neglecting inertia (implies terminal velocity), is written as the difference form of the time integral of velocity

$$\delta \vec{x} = \vec{\vec{v}}_{B}\, \delta t \qquad (2\text{-}4)$$

$\delta \vec{x}$ ≡ vector change in position

$\vec{\vec{v}}_{B}$ ≡ average velocity

δt ≡ time increment

The buoyant force is given (for nearly spherical bubbles)

$$\vec{F}^{B} = \left[\frac{4}{3}\,\pi\, R_{B}^{3}\, g\,(\rho_{\ell} - \rho_{g})\right] \hat{e}_{g} \qquad (2\text{-}5)$$

Consideration of the effect of a surface tension gradient on bubble motion requires conceptual investigation of the principles of interfacial phenomena. The interface is a thin film which is elastic but not plastic (it may not flow), Reference 6, for no circulation within the bubble. The bubble is treated as an inertialess void. The normal traction, therefore, establishes the surface topology and has no accelerative

effect on the bubble. A confined liquid segment, on the other hand, would have an induced pressure gradient corresponding to the surface tension gradient and would cause the liquid to flow. The tangential tractions will accelerate the bubble since the interfacial surface cannot flow. The result for an axially symmetric surface is given by Reference 4 as

$$\vec{F}^{ST} = - \iint \Delta_{\underline{\underline{T}}} \cdot \vec{n}_T \, dS \equiv \text{acceleration due to surface effects} \qquad (2\text{-}6)$$

$\Delta_{\underline{\underline{T}}} \equiv$ net surface traction tensor

$\vec{n}_T \equiv$ unit tangent vector to surface

For an axially symmetric surface and surface tension gradient

$$\Delta_{\underline{\underline{T}}} \cdot \vec{n}_T = (\vec{\nabla} \sigma \cdot \vec{n}_T) \vec{n}_T \qquad (2\text{-}7)$$

For small changes in bubble radius with polar angle

$$\Delta_{\underline{\underline{T}}} \cdot \vec{n}_T \cong \left[\frac{\partial \sigma}{\partial R_B} \left(\frac{1}{R_B} \frac{\partial R_B}{\partial \theta} \right) + \frac{1}{R_B} \frac{\partial \sigma}{\partial \theta} \right] \vec{n}_\theta \qquad (2\text{-}8)$$

The bubble radius for an axial symmetric bubble is given by the balance of normal surface traction across the bubble surface, this is constant since the surface is not growing,

$$\frac{\sigma}{R_B} = \frac{\sigma_o}{R_{B_o}} = \text{constant} \qquad (2\text{-}9)$$

which defines the bubble radius or topology. For an axial temperature field

$$\sigma = \sigma_o + R_B \cos\theta \frac{\partial \sigma}{\partial T} \frac{\partial T}{\partial Z} \qquad (2\text{-}10)$$

$$\frac{\partial \sigma}{\partial R} = \cos\theta \frac{\partial \sigma}{\partial T} \frac{\partial T}{\partial Z} \qquad (2\text{-}11)$$

From Equation (2-9)

$$\frac{1}{R_B} \frac{\partial R_B}{\partial \theta} = \frac{R_{B_o}}{\sigma_o R_B} \frac{\partial \sigma}{\partial \theta} \qquad (2\text{-}12)$$

Equation (2-8) becomes

$$\underline{\Delta}_T \cdot \vec{n}_T \cong \frac{1}{R_B} \frac{\partial \sigma}{\partial \theta} \left[\cos\theta \frac{\partial \sigma}{\partial T} \frac{\partial T}{\partial Z} \frac{R_{Bo}}{\sigma_o} + 1 \right] \vec{n}\theta \tag{2-13}$$

From symmetry, only the axial component of force survives

$$F_Z^{ST} = \iint (\nabla\sigma \cdot \vec{n}_T) \sin\theta \, ds \tag{2-14}$$

$$\frac{1}{R_B} \frac{\partial \sigma}{\partial \theta} \cong - \sin\theta \frac{\partial \sigma}{\partial T} \frac{\partial T}{\partial Z} \tag{2-15}$$

$$F_Z^{ST} = - 2\pi \int_o^{\pi} R_{Bo}^2 \sin^3\theta \frac{\partial \sigma}{\partial Z} \left[\cos\theta \frac{\partial \sigma}{\partial T} \frac{\partial T}{\partial Z} \frac{R_{B_o}}{\sigma_o} + 1 \right] d\theta \tag{2-16}$$

To first order, Equation (2-16) yields

$$F_Z^{ST} = - \frac{8\pi}{3} \frac{\partial \sigma}{\partial T} \frac{\partial T}{\partial Z} R_{B_o}^2 \tag{2-17}$$

Equation 2-17 is for a nearly spherical gas volume with a single surface (bubble). The vector form of (2-17) is

$$\vec{F}^{ST} = - \frac{8\pi}{3} \frac{\partial \sigma}{\partial T} R_{B_o}^2 \vec{\nabla} T \tag{2-18}$$

The drag force is given by

$$\vec{F}_D = - C_D \rho_\ell \frac{v_B^2}{2} (\pi R_B^2) \hat{e}_v \tag{2-19}$$

The velocity vector direction is given by the vector sum of forces (Equation 2-3)

$$\hat{e}_v = \frac{\{ \vec{F}^{ST} + \vec{F}^{B} \}}{| \vec{F}^{ST} + \vec{F}^{B} |} \tag{2-20}$$

In order to define the drag coefficient, it is necessary to review the kinematics of bubble drag. Three regions of interest are considered

I Spherical Particle
II Nearly Spherical Particle
III Deformable Body and the Transition Region

Region I is commonly known as Stokes drag region for spheres; the Reynolds number interface for Regions I and II occurs at Re ≈ 2, Reference 8. Region II is for nearly spherical particles and is the same functional relationship as Region I with different constants. The Reynolds number interface for Regions II and III is a function of fluid parameters and is defined by the intersection of the drag function in Region II with the functional relationship in Region III. Typical values of Re at the intersection are 80-400. The evaluation of the region separation and functional dependences in each region are based on extensive study and comparison of data contained in References 8 and 9. Considerable scatter and conflict in data preclude a more definitive evaluation. In Regions I and II, the drag coefficient is a simple function of Reynolds Number.

$$C_D = a\,Re^n \tag{2-21}$$

The velocity is defined by

$$v_B = \left[\frac{\mu_\ell}{2R_B \rho_\ell}\right]\left[-\frac{64\,R_B^2\,\rho_\ell\,\frac{\partial\sigma}{\partial T}(\vec{\nabla} T \cdot \hat{e}_v)}{3\,a\,\mu_\ell^2} + \frac{32\,R_B^2\,\rho_\ell\,g\,(\rho_\ell - \rho_g)(\hat{e}_g \cdot \hat{e}_v)}{3\,a\,\mu_\ell^2}\right]^{\frac{1}{2+n}} \tag{2-22}$$

The value for "a" of 24 provides reasonable data correlation for Region I, with n = -1. For Region II, a = 19.7 and n = -.725 are appropriate.

Region III is associated with the onset and growth of surface deformation due to tangential shear stresses. The region embodies both the initial oblate deformation and the final "hemispherical cap" configuration. The drag coefficient is a function of the ratio of accelerative forces ($\vec{F}^B + \vec{F}^{ST}$) to normal surface tension traction; for only buoyant forces, this is the Eötvös or Bond number.

$$N_E \equiv \frac{3\,|\vec{F}^B + \vec{F}^{ST}|}{\pi\,R_B\,\sigma} \tag{2-23}$$

$$C_D = C_\infty\,(1 - e^{-\lambda N_E}) \tag{2-24}$$

The exponential relaxation of Equation (2-24) accommodates the transition to the totally deformed hemispherical cap state. Values of $C_\infty = 2.64$ and $\lambda = 0.13$ were found to give the best correlation with References 8 and 9. Using n = 0 and $a = C_D$ in Equation(2-22), the velocity is prescribed for Region III.

In Region III, the acceleration due to surface tension gradient (temperature field) is reduced because the topological deformation alters the surface integral and traction in Equation (2-6) and introduces anisotropic components. However, this force is only important in low-g buoyancy situations; therefore, the alteration for region dependence is neglected.

The effect of finite medium on the velocity is approximately treated by considering the mass conservation equation of the liquid surrounding the bubble in the limited region. The increased relative velocity around the bubble increases the drag and results in a reduced velocity for the bubble in the confined region.

$$\frac{v_{B_A}}{v_{B_\infty}} \cong v_{B_\infty}(1 - \alpha) \tag{2-25}$$

where α is the local area fraction of bubbles.

2.2.2 BUBBLE ENERGY EQUATION FOR A SINGLE BUBBLE — Thermodynamic evolution of a bubble is described by a differential form of the first law energy equation. The gaseous phase inside the bubble is considered to be saturated at the pressure corresponding to the external pressure plus the surface traction. Energy transport (heat and/or mass transfer) between the bubble and liquid phase is considered.

$$0 = m_2 u_2 - m_1 u_1 + \delta m_c \bar{h}_T + \delta m_Q \bar{h}_T - \delta m_V \bar{h}_T + \delta(Pv) \tag{2-26}$$

for time 1 to time 2, where,

$$\bar{h}_T \equiv \begin{cases} \bar{h}_g \sim \delta m_c < 0, \ \delta m_Q < 0, \ \delta m_V > 0 \\ \bar{h}_{fg} \sim \delta m_c > 0, \ \delta m_Q > 0, \ \delta m_V < 0 \end{cases}$$

Continuity of bubble mass yields

$$m_2 - m_1 = \delta m_V - \delta m_Q - \delta m_c \tag{2-27}$$

It is assumed that the bubble remains at saturated gas conditions.

2.2.3 WAKE EFFECTS — In the study of bubble populations, the velocity field behind a bubble (wake) must be considered in the velocity prescription of bubbles traveling in succession. As an approximate approach, a superposition of wake velocities which interfere with a particular bubble is used. This is quite reasonable for moderately dense populations because the wake relaxes as $(x/d)^{-2/3}$ for axisymmetric bubbles.

The velocity of bubble "i" is given by

$$\vec{v}^{\,i}_B = \vec{v}^{\,i}_{B_A} + \sum_{j \neq i} \langle \vec{v}^{\,ji}_w \rangle$$

where

$\vec{v}_w^{ji}$ ≡ wake velocity which interacts with bubble "i" from bubble "j"

The velocity field in the wake of axisymmetric bodies is expressed by a vector representation of the wake velocity

$$\vec{v}_w^{ji} = f_1^{ji} \vec{v}_{B_A}^{j} + f_2^{ji} \left[\frac{\vec{R}_{ji}}{|\vec{R}_{ji}|} - \frac{(\vec{R}_{ji} \cdot \vec{V}_{B_A}^{j})}{|\vec{R}_{ji}| \, |\vec{V}_{B_A}^{j}|} \vec{v}_{B_A}^{j} \right] \tag{2-28}$$

where

$\vec{R}_{ji} \equiv \vec{x}^{j} - \vec{x}^{i}$ ≡ relative vector coordinate of bubble (j) with respect to bubble (i)

$\vec{x}$ ≡ position vector of bubble

f_1^{ji} ≡ functional dependence of axial velocity in wake of the relative distance $|\vec{R}_{ji}|$

f_2^{ji} ≡ functional dependence of radial velocity in wake on the relative distance $|\vec{R}_{ji}|$

The terms axial and radial are defined by the velocity vector of the lead bubble (j).

The velocity field behind a single body with axial symmetry has been investigated, Reference 10, for turbulent wakes. The consideration of only turbulent wakes is reasonable since laminar wakes occur only for very small bubbles or low velocities where wakes are not important; also, the laminar wake is similar to a turbulent wake in its attentuation, $(x/d)^{-1}$, References 6 and 11.

The functions f_1^{ji} and f_2^{ji} are

$$f_1^{ji} = |\vec{v}_{B_A}^{j}| \left[0.202 \, C^{-0.8} \right] \left[\frac{C_D \pi R_B^{j2}}{x_{ji}^2} \right] \left[1 - \eta_{ji}^{3/2} \right]^2 \tag{2-29}$$

$$f_2^{ji} = |\vec{v}_{B_A}^{j}| \left[0.0825 \, C^{-1.067} \right] \left[\frac{C_D \pi R_B^{j2}}{x_{ji}^2} \right]^{2/3} \eta_{ji} \left[1 - \eta_{ji}^{3/2} \right]^2 \tag{2-30}$$

where

$$x_{ji} \equiv \frac{\vec{R}_{ji} \cdot \vec{V}_{B_A}^{j}}{|\vec{v}_{B_A}^{j}|} \equiv \text{projection of relative position vector on velocity direction of lead bubble} \tag{2-31}$$

$$\eta_{j1} = | \vec{R}_{j1} - x_{j1} \vec{v}^{j}_{B_A} | \qquad b \equiv \text{normalized projection of relative position vector on the direction normal to velocity of the lead bubble} \tag{2-32}$$

$$b \equiv 1.222\ C^{-0.267}\ (C_D \pi R_B^{j2}\ x_{j1})^{1/3} \tag{2-33}$$

The constant "C" is determined by experimental correlation. A value of C = 0.288 was obtained using data in Reference 12.

2.2.4 AGGLOMERATION AND TANK WALL INTERACTION — Inter-bubble agglomeration (coalescence) and bubble, liquid-ullage surface coalescence is represented by two equations

$$| \vec{R}_{j1} | \leq (R_B^i + R_B^j) + \delta_{IMP} \tag{2-34}$$

$\delta_{IMP} \equiv$ impact parameter for bubble collisions

$$| \vec{R}_{is} | \leq R_B^i + \delta^s_{IMP} \tag{2-35}$$

$\delta^s_{IMP} \equiv$ impact parameter for bubble-surface collision

$\vec{R}_{is} \equiv$ vector from bubble center normal to liquid-ullage surface

Equations (2-34) and (2-35) define conditions for agglomeration to occur; for inter-bubble collision, the resulting bubble is positioned at the center of of two original bubbles. Observation of coalescence indicates that

$$\delta^s_{IMP} = \delta_{IMP} = 0$$

Bubble collisions with the confining walls of the tank result in one of two possible situations: free slip, no slip.

$$\text{Free Slip} \sim \vec{v}_B \cdot \vec{n} \Big|_{WALL} = v_{B_n} \Big|_{WALL} = 0$$

$$\text{No Slip} \sim \vec{v}_B \Big|_{WALL} = 0$$

In the first situation, the bubble hits the wall and travels along a geodesic of the surface; for the second situation, the bubble strikes the wall and remains at the point of impact.

Another consideration is that the wall may be porous and the bubble could possibly escape; this is determined by the relation of the normal force of the bubble at the container wall to the surface tension retardation force provided by the wall pores. If the normal force is greater than the combined surface tension forces of all involved pores, then the bubble "escapes" and is lost forever; if the normal force is less, the bubble is retained.

2.2.5 VAPORIZATION — There are two mechanisms for vapor generation: nucleate boiling, and "bulk" boiling. For nucleate boiling, the site, the time dependent initial radius, and the time dependent frequency of production are input to the program. The mass of vapor produced is subtracted from the liquid phase and new bubble is born.

Boiling which is the result of change in thermodynamic state of the liquid (bulk), e.g., pressure decay and convective heat transfer, is added to the existing voids, including the ullage space, in proportion to liquid-gas interfacial areas.

$$\delta m_V^i = \frac{C_A (4 \pi R_B^{i2}) \delta m_{LV}}{\left[A_s + 4 C_A C_{DEG} \sum_j (\pi R_B^{j2}) \right]} \qquad (2\text{-}36)$$

where

δm_{LV} = liquid phase mass change due to vaporization

A_s = liquid-ullage interface area

δm_V^i = mass addition to i^{th} bubble

C_A ≡ arbitrary weighting factor

C_{DEG} ≡ degeneracy factor for considering only a sector

The parameter C_A permits alteration in the partitioning of vapor production between bubbles and the ullage space. The degeneracy factor is an artifice which represents an axisymmetric container and void distribution as a degenerate sector of the cross section. In other words, only the evolution of voids in one degenerate sector need be considered if all forces obey the same symmetry rules as the container and the voids do not outgrow this sector. The program uses C_{DEG} to keep track of gas, liquid phase and volume changes to insure the satisfaction of conservation requirements.

$$C_{DEG} = \frac{2 \pi}{\text{SECTOR ANGLE (RADIANS)}} \equiv \text{INTEGER QUANTITY} \qquad (2\text{-}37)$$

Observations of boiling due to pressure reduction indicate that existing voids increase appreciably in size and that some new nucleation sites appear on the walls; however, there is no evidence that new bubbles are created internal to the liquid phase providing that no incipients are present, e.g. gases in solution, solid particles, and other contaminants. The latter could be input as additional nucleation sites.

Liquid Energy Conservation and Level Determination. The liquid phase energy conservation is defined by a differential first law energy equation. The pressure history is a given function of time (input).

$$\delta Q_\ell = m_{\ell_2} u_{\ell_2} - m_{\ell_1} u_{\ell_1} + \bar{h}_\ell \delta m_o + \bar{h}_{fg} \delta m_{LV} \qquad (2\text{-}38)$$

where

$\delta Q_\ell \equiv$ convective or conductive heat transfer to liquid (input per unit liquid height)

$\delta m_o \equiv \delta m_{FO} - \delta m_c - \delta m_Q$, where δm_{FO} is the liquid outflow, δm_c is the mass transfer due to bubble vaporization, δm_Q is the mass transfer due to heat transfer to the liquid phase.

Mass conservation yields,

$$m_{\ell_2} - m_{\ell_1} = \delta m_o + \delta m_{LV} \qquad (2\text{-}39)$$

Because of the arbitrary surface angle (function of time) and the various axisymmetric tank configurations, the liquid level is calculated every time step by an iterative method. The convective or conductive heat transfer to the liquid is input per unit liquid height; therefore, the program explicitly calculates the feedback effect of changing heat input with liquid level.

2.2.6 RECOMMENDATIONS — Bubble motion predictive capability has been verified experimentally by correlation with air bubbles rising in a water bath under Contract NAS 1-8494. This successful correlation suggests that the EVOLVE program may be used for bubble dynamics problems which arise in capillary device design.

Suggested additions to the program to extend its usefulness are superposition of liquid velocity fields due to convective and boundary layer flows, treatment noncondensible gas components and more general consideration of tank geometries including baffles.

2.3 RESIDUAL PROPELLANT PREDICTION

In order to properly evaluate surface tension propellant control systems, it is necessary to know the amount of unusable propellant present in the tank at vapor pullthrough. Prediction of residuals requires knowledge of the interface shape within the start basket and remainder of the tank and relative liquid levels in both volumes. The work presented here is a condensation of the pullthrough and residual analysis presented in Reference 2.

Interface shape was considered for both normal and low gravity, with baffled and unbaffled tank outlets, and centrally positioned and off-axis drains.

2.3.1 INTERFACE SHAPE. The general problem of interface shape during tank draining can be viewed with the aid of the familiar triangle shown below. Assuming that viscous forces are always small, the three major regimes are:

1. Low inertia forces — characteristic parameter: Bond number.
2. Low surface forces — characteristic parameter: Froude number.
3. Low gravity — characteristic parameter: Weber number.

When inertia forces are low, suction dip can be assumed to be absent and the volume of residual propellant in a draining tank is just the meniscus volume. For liquids with a contact angle of zero (cryogenic fluids included), Figure 2-8 gives the meniscus volume.

Froude number simulation is valid when surface tension forces are small. This is the condition for most of the theoretical and experimental work done in tank draining. The liquid is characterized by a generally flat interface except near the drain.

In low gravity fields, Weber number correlations have been found to represent the draining phenomenon. Drop tower experiments show major differences in the phenomenon for low and high Weber numbers.

There appears to be no straightforward way to combine the results for these limiting conditions into one or even several simple forms. Furthermore, the geometry thus far has been limited to cylindrical tanks with centralized drains. Inclusion of the effects of screens in the flow path will be discussed subsequently. At this point, even for the cylindrical tanks without screens or baffles, we are forced to predict residuals based on the assumption that one of the three controlling forces is negligible.

2.3.2 FROUDE NUMBER DRAINING (SURFACE TENSION SMALL). Vapor pullthrough in unbaffled tanks at 1-g has received considerable attention in recent years, and the theoretical developments have been favorably correlated by experimental data. The more complex situation of vapor pullthrough in tanks at near zero-g and with

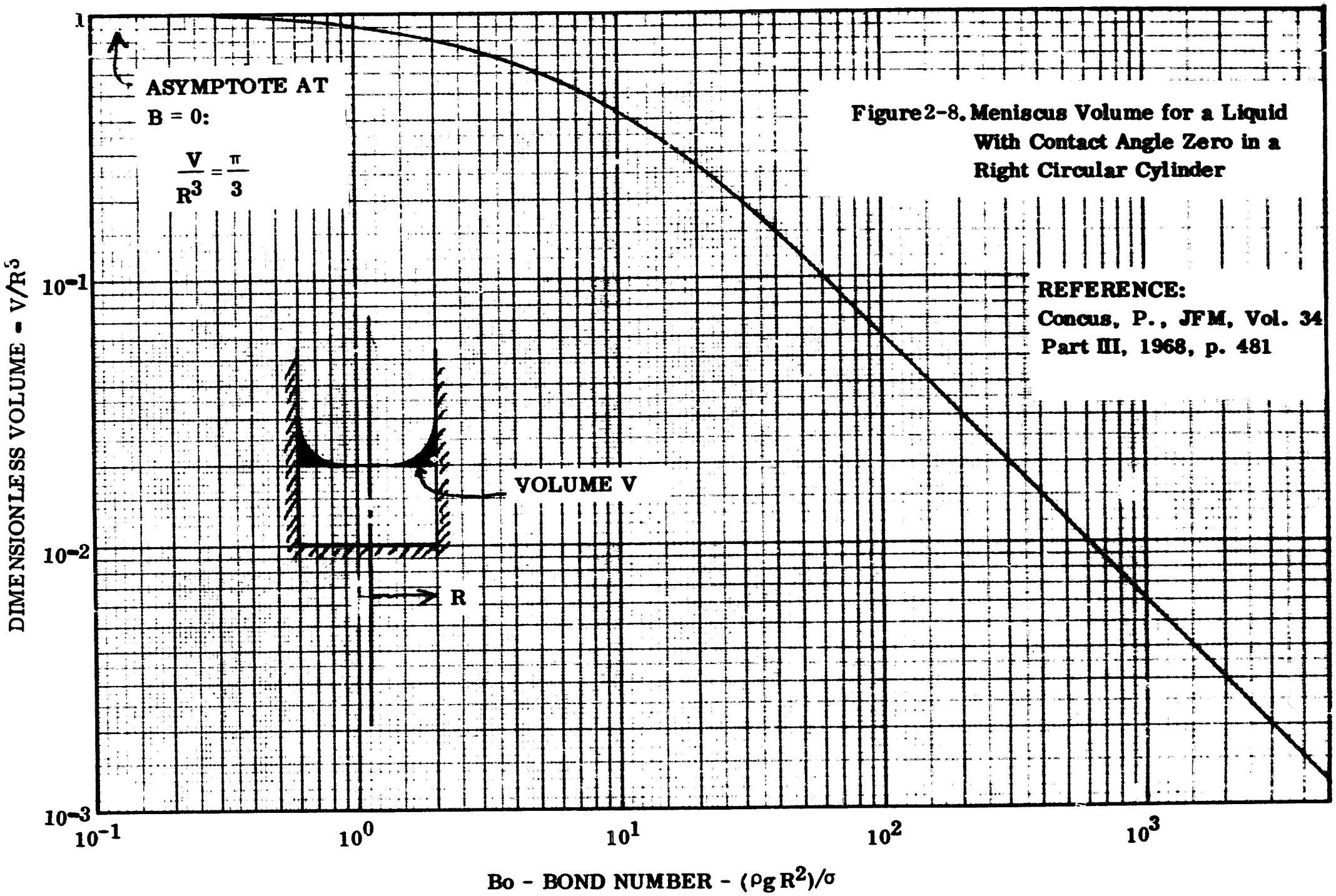


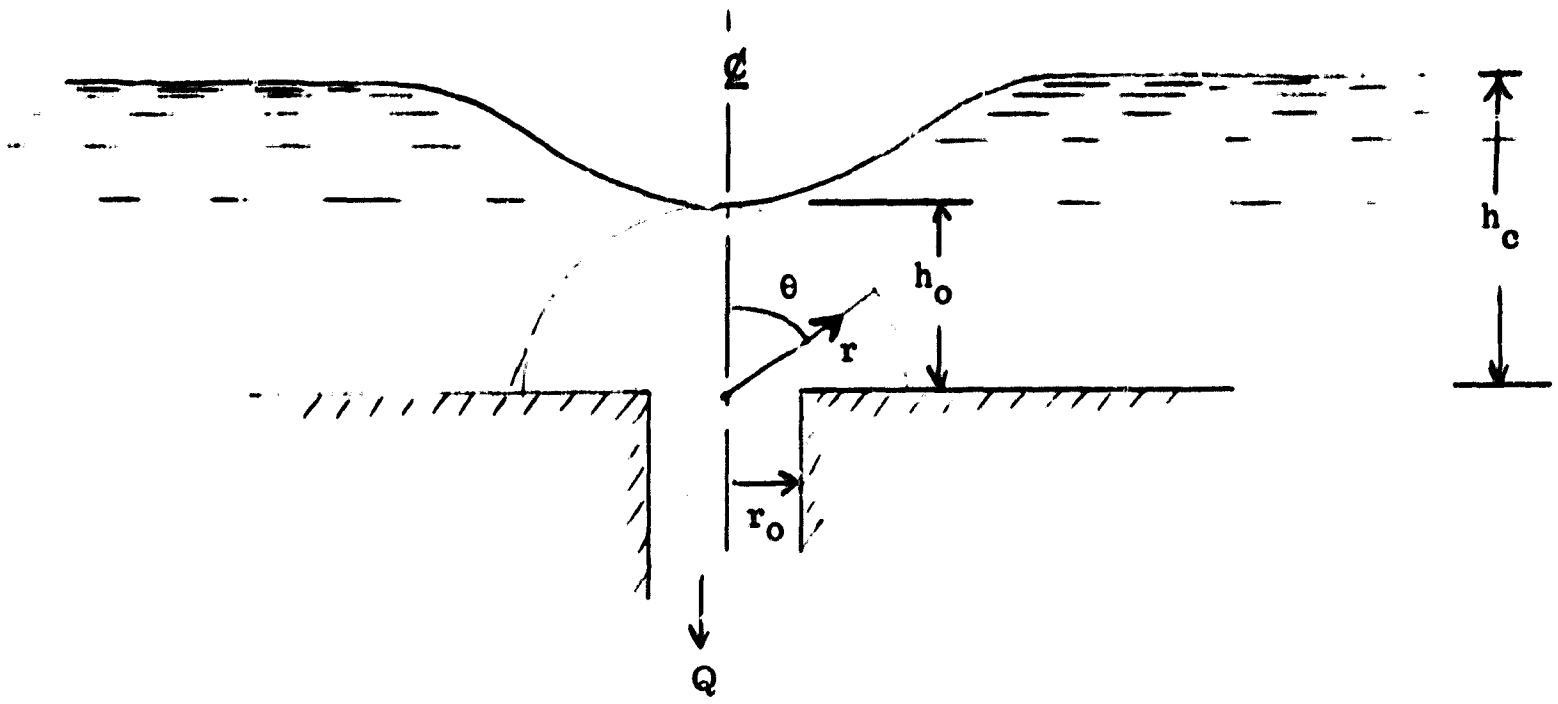
Figure 2-8. Meniscus Volume for a Liquid With Contact Angle Zero in a Right Circular Cylinder

Figure 2-8. Meniscus Volume for a Liquid With Contact Angle Zero in a Right Circular Cylinder

baffles has not had the good fortune of much theoretical treatment or experimental measurement. In this discussion the more familiar, simpler problem will be reviewed as an introduction.

At the outset it should be noted that the problem of vortex formation is ignored. Past experience has shown that, although vortexing is a serious problem, it can be prevented. Such precautionary measures are assumed to have been implemented.

Suction dip and the vapor pullthrough phenomena at 1-g have been treated (and apparently successfully) by considering the incipient pullthrough tank flow to be steady, inviscid, and one-dimensional. A justification of these assumptions is given in Reference 2. The usual terminology is depicted below.



Suction Dip Model Terminology

If the drain diameter is very small compared to the tank diameter, the flow pattern can be simulated by a point sink in a spherical coordinate system. Laplace's equation $\nabla^2 \varphi = 0$ then has the solution $\varphi = c/r$ or $v_r = -c/r^2$.

Assuming an inviscid fluid and $h_c \gg r_o$.

$$\frac{Q}{g h_c^{\,5}} = 6.5, \quad \text{where } h_c \text{ is the height when the velocity of the free surface opposite the outlet is much greater than the velocity of the surface at the tank wall.} \qquad (2\text{-}40)$$

When $r_o \gg h_c$ the representation of the drain as a point sink fails. This limiting case was examined in Reference 13, nevertheless, and a result was obtained. A different approach will be taken here to derive a similar relationship (at 1-g).

Pullthrough is again assumed to occur instantly so that when it occurs, flow into the drain can be represented by fluid spilling over an abrupt step. It is known that maximum flow over a "fall" occurs at the critical depth of the fluid (Froude number unity). Therefore, when the fluid recedes from this level, the drain will become "choked." The problem is to relate the critical depth at the drain radius to the drain rate. An inviscid open channel model is assumed, (see Figure 2-10). For one-dimensional flow parallel to the bottom of the tank

$$\frac{Q_c^2}{r_o^2 g h_c^3} = 11.8 \qquad (2\text{-}41)$$

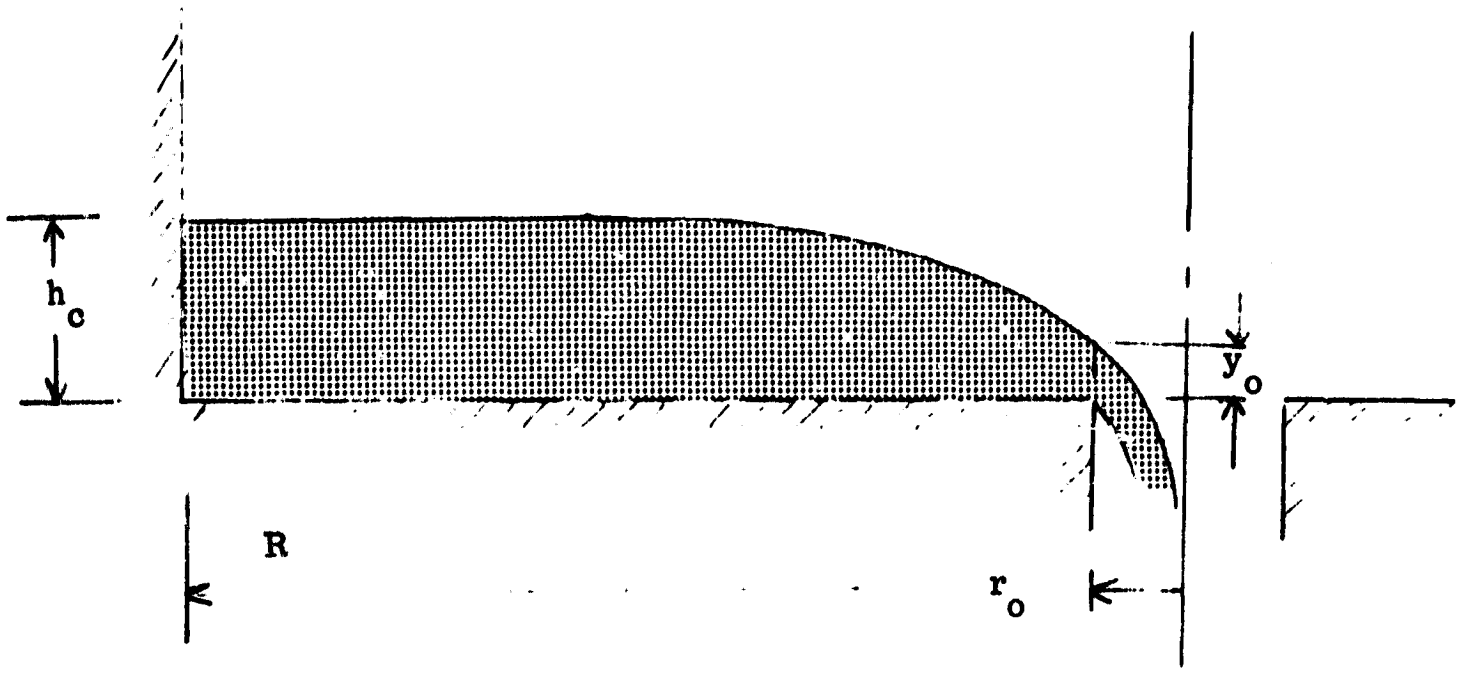


Figure 2-9. Open Channel Model Nomenclature

Data from Reference 2-14 with $4.63 \leq D/d \leq 10$ is reproduced in Figure 2-10. To compare Equations (2-40) and (2-41) with this data, the variables must be rearranged. Equations (2-40) and (2-41) can be written respectively as:

$$h_c/D = .629\ F^{1/5}\ (d/D)^{1/5},\ h_c \gg r_o \qquad (2\text{-}42)$$

$$h_c/D = .593\ F^{1/3}\ (D/d)^{1/3},\ h_c \ll r_o \qquad (2\text{-}43)$$

where $d = 2\ r_o$, D = tank diameter, and $F = V^2/gd$, with V = mean fluid velocity in tank based on tank cross sectional area.

Since the data presented in Reference 14, are very well represented by Equation 2-40, they are not shown in Figure 2-10. One can see that for $D/d > 5$, Equation (2-42) fits both sets of data. No known data exist in the low Froude number range, but is is presumed that Equation (2-43) is valid for values of F lower than the point of intersection of curves for Equations (2-42) and (2-43), since h_c becomes smaller relative to r_o in this range.

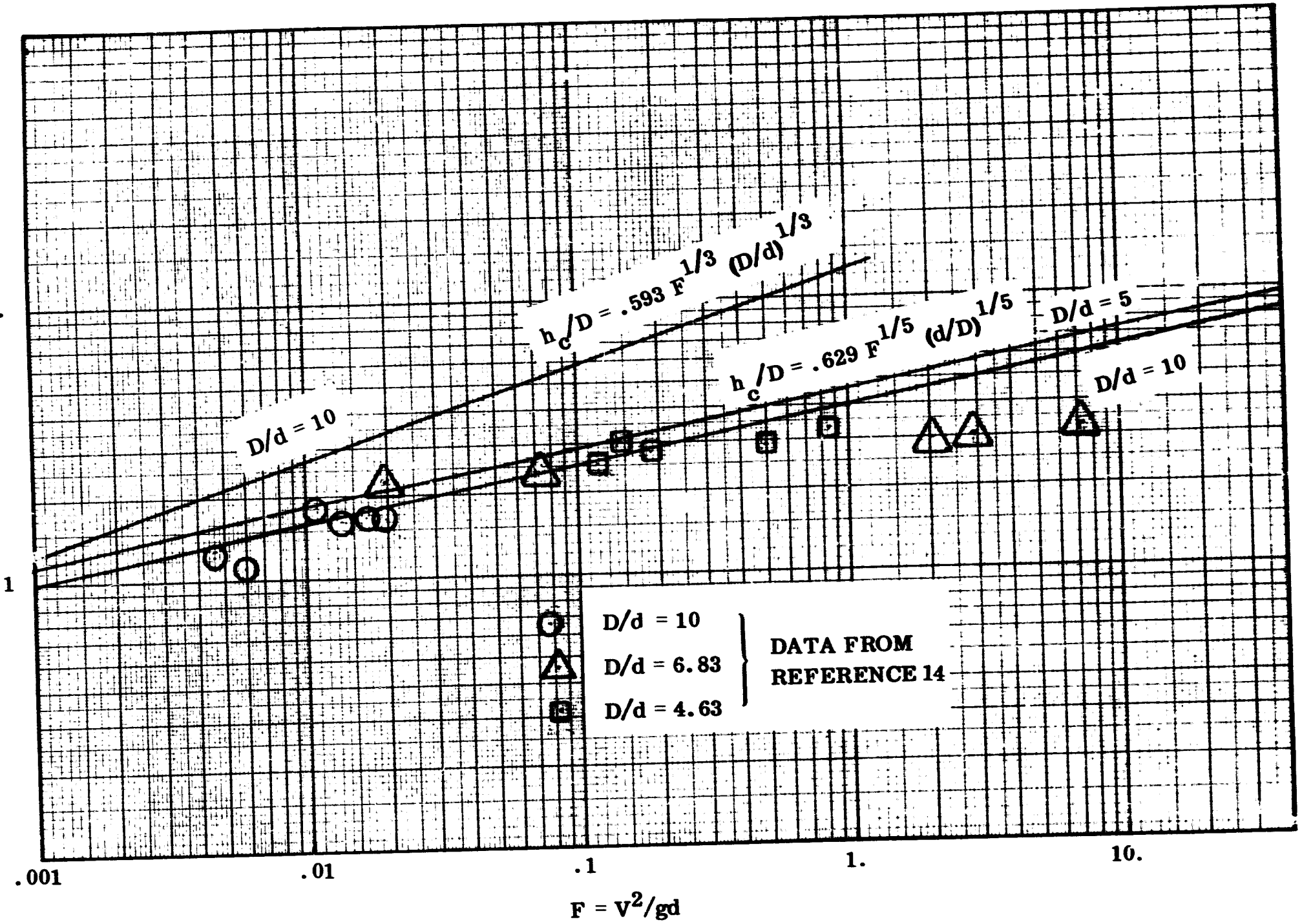


Figure 2-10. Comparison of Suction Dip Correlations.

BAFFLED OUTFLOW. Consider Figure 2-11

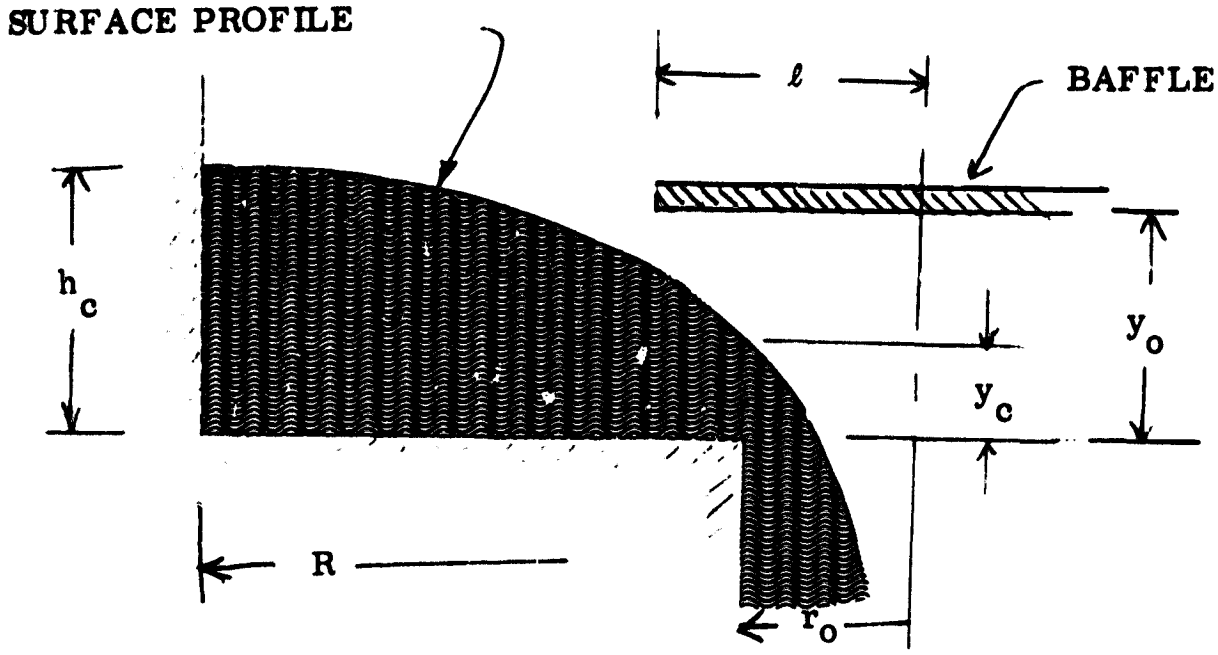


Figure 2-11. Pullthrough With Baffled Drain - Terminology

The outflow pattern can be forced to follow the open channel flow-over-a-fall model only if the baffle intersects the critical surface profile as in Figure 2-11. If $\ell = r_o$, h_c can be decreased only if $y_o < y_c$. In this case $h_c = 3/2\ y_o$. If $\ell \geq r_o$ then h_c will always be less than $3/2\ y_o$ as long as $y_o < y_c$. Assuming that @ $r = \ell$ the flow pattern is equivalent to [illegible] over a fall where $r = \ell$ is the point at the edge of the fall. If this is the case, then the pullthrough height for the drain configuration of Figure 2-11 is given by:

$$Q_c^2/\ell^2\ g\ h_c^3 = 11.8 \qquad (2\text{-}44)$$

(remembering that $y_o < y_c$). For the configuration shown in Figure 2-11, the baffle must be lowered to below y_c in order to reduce residuals from the unbaffled case. Ref. 15 analyzes another baffle configuration shown in Figure 2-12.

If the flow in Figure 2-12 is similar to flow over a fall, a development identical to the previous one gives:

$$\frac{Q^2}{g\ h_c^3\ (\ell + \delta)^2} = 11.8$$

Reference 16, attacking the problem in another way arrives at:

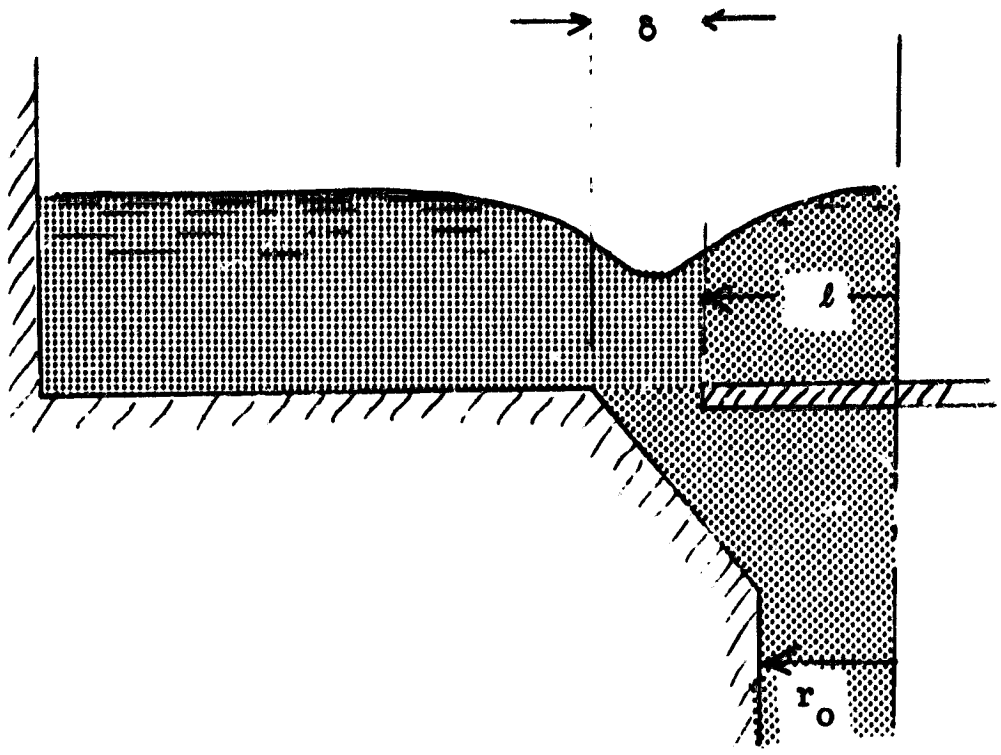


Figure 2-13. Pullthrough With a Sump and Baffled Drain

$$\frac{Q^2}{g\, h_c^{\,3}\, (2\ell + \delta)^2} = 11.8$$

To check the baffling efficiency we can compare Equations (2-40) and (2-44):

$$\frac{h_c^{\,5}\,(\text{unbaffled})}{h_c^{\,3}\,(\text{baffled})\,\ell^2} = 1.82$$

A simple yet very effective way to reduce residuals might be to install a screen over the inlet to a very wide drain line.

If the sump in Figure 2-13 is properly designed, flow across the screen will be reasonably uniform and the effective drain radius will then be r_*. Comparing critical height values h_c for the case when $r_* = 8\, r_o$, using (2-41), one can see that

$$\frac{h_c\,(\text{screen})}{h_c\,(\text{no screen})} = \left(\frac{r_o}{r_*}\right)^{2/3} \sim 8^{-2/3} = \frac{1}{4}$$

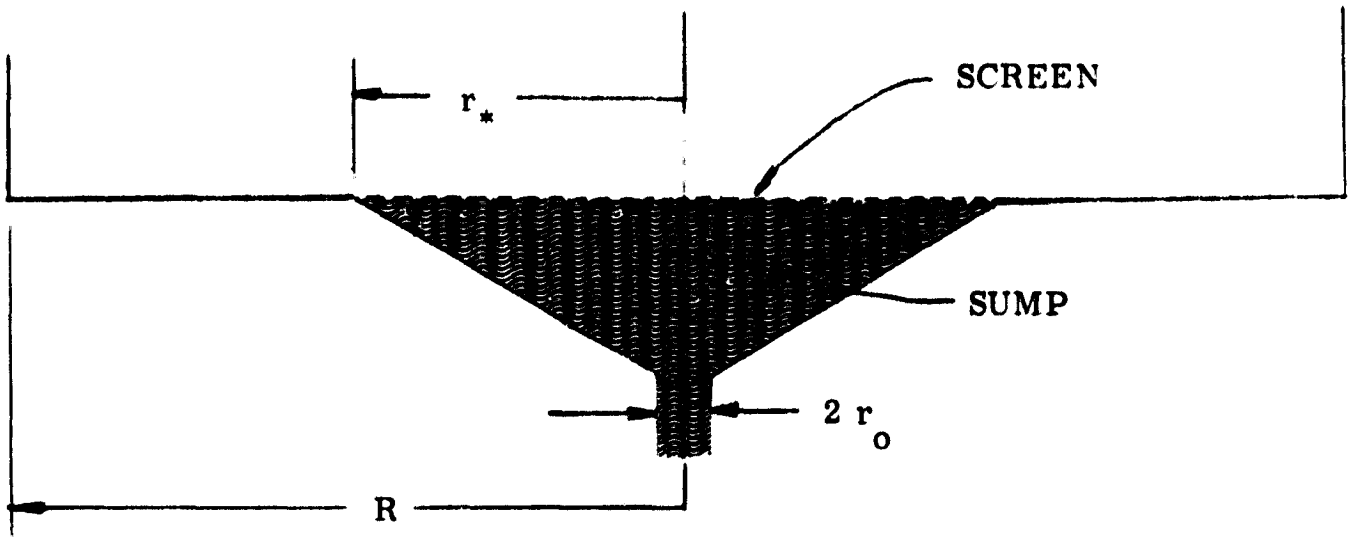
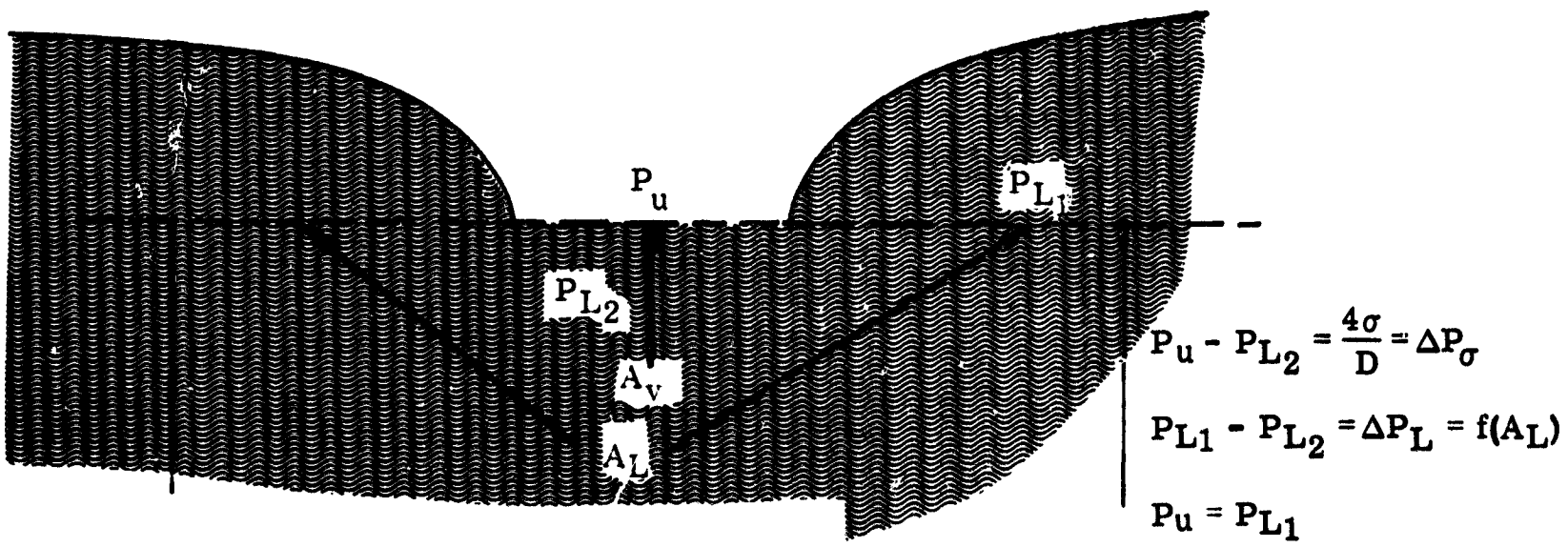


Figure 2-13. Pullthrough With Sump and Screen Over Drain

In addition to smoothing out velocity gradients in the draining fluid, screens provide additional capacity to retard vapor pullthrough. Wetted screens will resist vapor penetration with a force equal to $4\sigma/d$. Thus, vapor hitting the screen with an impingement force of $\rho g A V_g^2$ will be constrained from passing through the screen by a force equal to $(4\sigma/d)A$ so that $\rho g V_g^2 < 4\sigma/d$ for vapor not to penetrate the screen.

The screen flow area must be of sufficient size so that the liquid flowing through the screen does not have a pressure drop exceeding that of the surface tension pressure drop.



As the surface falls due to the draining, more area will be covered by vapor. The liquid pressure drop will thus increase due to the increased velocity of the liquid flowing through the screen. A_L will be reduced until the liquid pressure drop, ΔP_L exceeds ΔP_σ. When this occurs, vapor will break through the screen and will subsequently be ingested into the engine.

2.3.3 ZERO-G DRAINING — References 17 and 18 show the effects of weightlessness on draining tank fluids. Four basic situations are analyzed: direct pressurant injection, and baffled and unbaffled drain openings. In addition to the highly curved interface brought about by the dominance of surface tension forces at low-g, a wall film phenomenon also appears to be instrumental in increasing tank residuals at the vapor ingestion point. The surface tension dominated interface effect will be discussed first, assuming that the curved liquid surface intersects the tank wall. Wall film flow will then be analyzed.

Low-G. In developing expressions for low-g pullthrough, Reference 16 be followed. As in Reference 13, a hemispherical control volume is placed over the drain (as shown on p. 2-27). Bernoulli's equation is applied along a streamline from a point away from the drain (∞) to the surface of the dip at the drain centerline (o).

$$P_\infty + \rho g h = P_o + \rho g h_o + 1/2\, \rho\, U^2 \qquad (2\text{-}45)$$

When the surface "dips" the fluid surface tension exerts restoring forces on the interface and the pressure difference between liquid and vapor is:

$$P_2 - P_1 = \sigma J$$

Where J is the local surface curvature. Expressing the drain flux as:

$$Q = 2\pi h_o^{\,2} U$$

and using (2-45), the liquid height is given as:

$$h - h_o - \frac{P_\infty - P_o}{\rho g} + \frac{Q^2}{8\pi^2 h_o^{\,4} g} \qquad (2\text{-}46)$$

At large distances from the dip $J_\infty \sim 1/R$, but at the dip the curvature is symmetric and

$$J_o \sim \frac{2}{R - \epsilon\,(h-h_o)}$$

where ϵ is a proportionality constant; now if $\epsilon = 1$ then:

$$\sigma\,(J_\infty - J_o) \sim -\frac{2\sigma}{R^2}\,(h - h_o) \qquad (2\text{-}47)$$

This expression, only an order of magnitude estimate, is developed in Reference 14, and is not presumed to be precise, but merely to indicate the functional dependence of surface tension in the equations.

Equation (2-46) becomes:

$$h = h_o + \frac{Q^2}{8\pi^2 g h_o^4 (1 + 2/B} \qquad (2\text{-}48)$$

where $B = \rho g R^2/\sigma$ (the Bond number).

Using the criterion for pullthrough, $dh/dh_o = 0$,

$$h_{oc}^5 = \frac{Q^2}{2\pi^2 g (1 + 2/B)} \qquad (2\text{-}49)$$

As before, putting (2-49) into (2-48) $h_c = 5/4\, h_{oc}$ and

$$\frac{Q_c^2}{g h_c^5 (1 + 2/B)} = 6.5 \qquad (2\text{-}50)$$

Using similar logic, Equation (2-41) for low g becomes:

$$\frac{Q_c^2}{r_o^2 g h_c^3 (1 + 2/B} = 11.8 \qquad (2\text{-}51)$$

Both these expressions reduce to the previous expressions for 1-g when $B \gg 1$. For ($B \ll 1$) Equations (2-50) and (2-51) becomes:

$$\frac{\rho Q_c^2 R^2}{h_c^5 \sigma} = 13.0 \qquad (2\text{-}52)$$

$$\frac{\rho Q_c^2 R^2}{r_o^2 h_c^3 \sigma} = 23.6 \qquad (2\text{-}53)$$

Low-G Baffled Draining

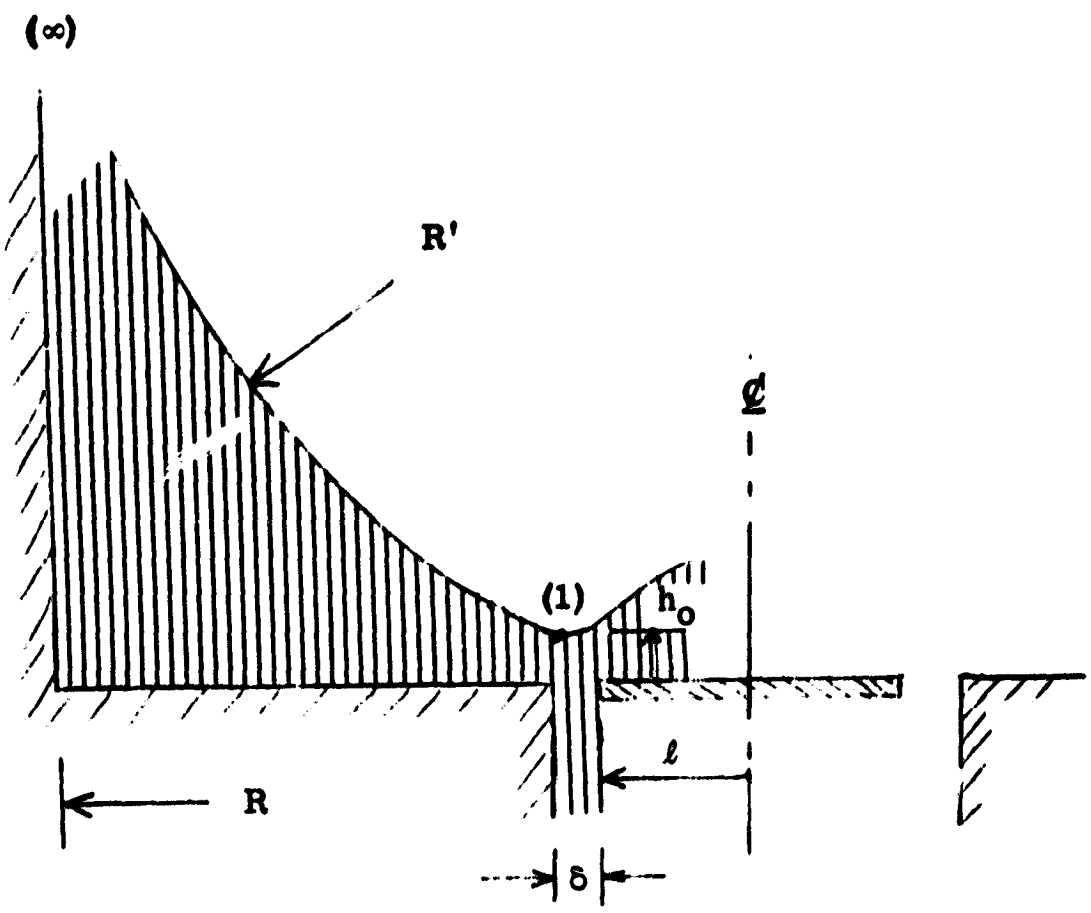


Figure 2-14. Low-G Baffled Draining

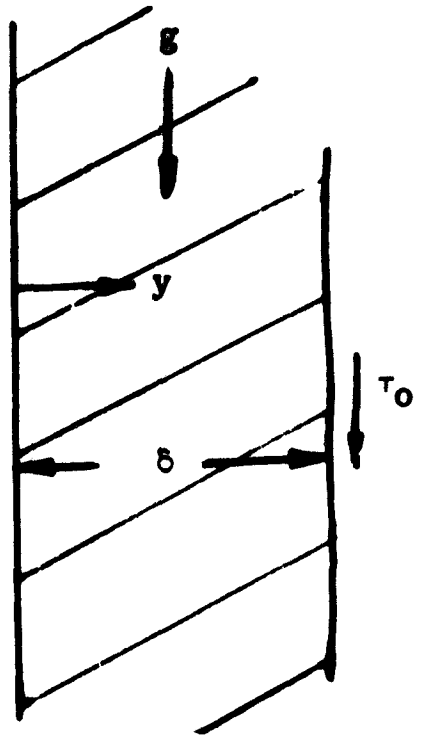
Consider the low-g analysis just described and the effect baffles have on draining as previously discussed on page 2-31;

$(h_c + \ell)^3 = 0.086 \frac{\rho R^2 Q^2}{\sigma \ell^2}$ was derived for low-g baffled draining.

Reference 18 shows a rather thick film of residual liquid on the walls of several drop tower test tanks. Since these films represent a large volume of liquid it is important to inquire about the conditions under which they exist. A simple two dimensional laminar model is assumed for the film, based on the idea that the central core of liquid, while leaving the tank, imparts a shear stress on the film/vapor interface. The gravity field is parallel to the wall.

Solving the equation of motion for this simple case gives the velocity profile

$$u = \frac{gy^2}{2\nu} + cy + D \qquad (2\text{-}54)$$



If the shear stress at the film surface is strong enough, the boundary conditions will be

$$u(o) = 0,\ u(\delta) = V$$

Equation (2-54) then becomes:

$$u = \frac{gy}{2\nu}(y - \delta) + V\frac{y}{\delta}$$

The average velocity in the film is

$$\bar{u} = \frac{1}{\delta}\int_o^\delta u\,dy = \frac{V}{2} - \frac{g\delta^2}{12\nu}$$

Reference 17 presents experimental data for outflow in zero gravity which, for Weber number larger than 2.0, can be correlated by

$$\left[\frac{V - V_m}{V}\right] h_i^{1.4} \cong 1.26 \qquad (2\text{-}55)$$

where h_i is the initial liquid level, before outflow, in tank radii. The parameter $(V-V_m)/V$ is referred to in Reference 17 as an interface distortion parameter. Since a relation can be obtained between $(V-V_m)/V$ and the film thickness, δ, the film residuals can be determined for low-g conditions at Weber numbers $(\rho V_m^2 R)4\sigma$ greater than 2. The relationship is found by

$$\frac{V - V_m}{V} = 1 - \frac{1}{V} (\bar{u} A_{film} + V A_{core})/A_{total}$$

Defining

$$\alpha = \frac{g R^2}{12 \nu V}$$

the solution is

$$\frac{V - V_m}{V} \quad \frac{\delta/R - 1/2 (\delta/R)^2 - \alpha(\delta/r)^3 (\delta/R - 2)}{1 - \alpha (\delta/R)^3 (\delta/R - 2)}$$

This is plotted in Figure 2-15

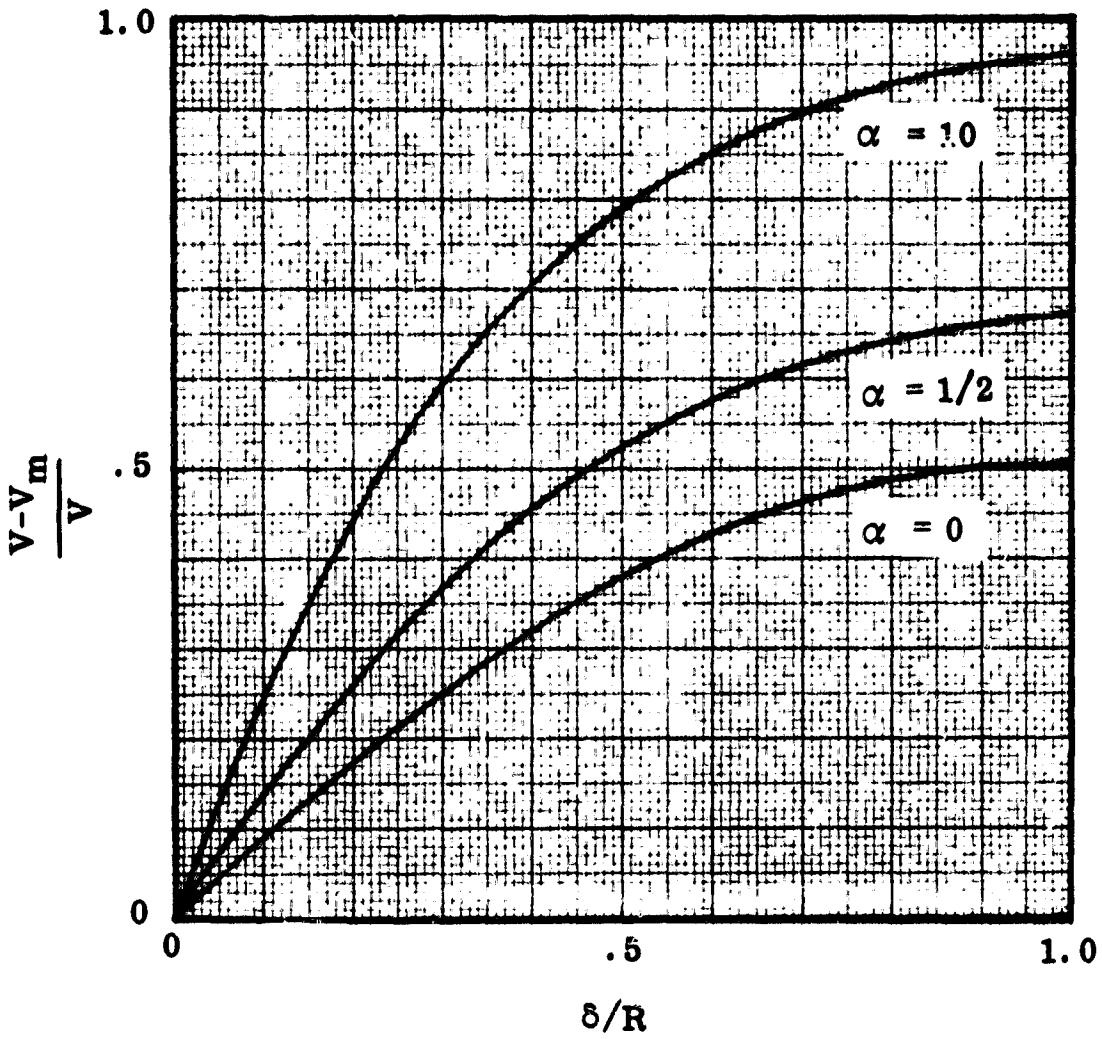


Figure 2-15. Film Thickness Versus Interface Distortion Parameter

To determine film residuals knowing the value of $(V - V_m)/V$ from Reference 17 or Equation (2-55) the value of δ/R is found from Figure 2-15. Note that as the gravity field becomes stronger or viscosity decreasing (increasing α) the film thickness decreases.

2.3.4 RESIDUAL VOLUME PREDICTION — A method has been developed for prediction of propellant residuals in vehicles with screened start baskets.

Equations describing the rate of change of volume (net flow rate) are written for each fluid region. The boundaries of these fluid regions are either solid or screened. By knowing the flow characteristics through the screens and by knowing the relationships between liquid level and volume, the set of differential equations can be solved simultaneously. A fourth order Runge-Kutta procedure with automatic step size adjustment has been used for this purpose, built into a computer program which supplies fluid and screen data, monitors the fluid levels, and checks screen flow regimes.

Figure 2-16 shows a simple tank and start basket configuration and will be used to describe the calculation procedure.

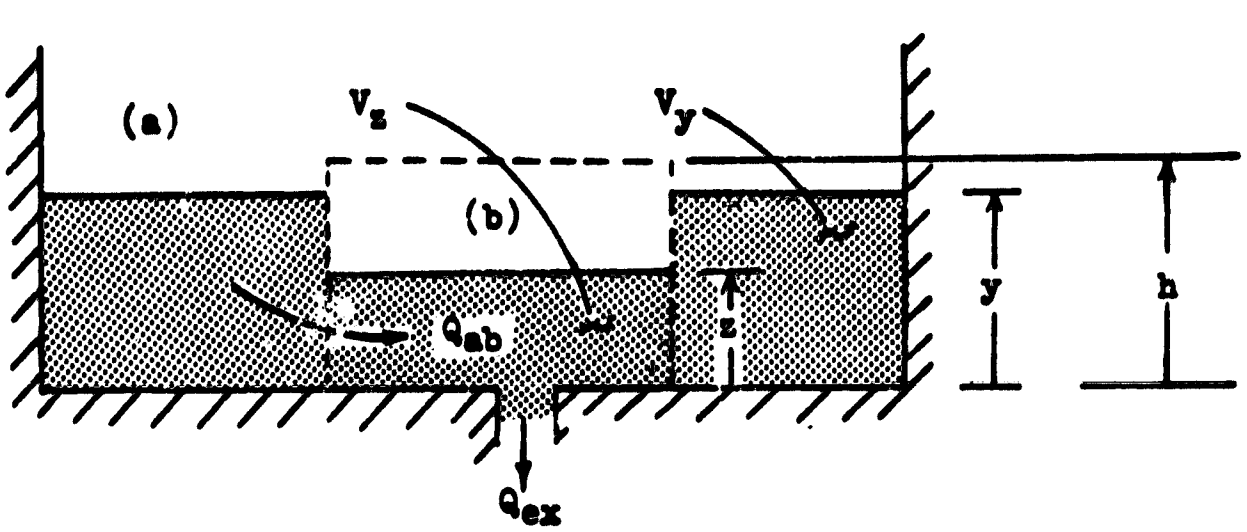


Figure 2-16. Schematic of Start Basket Draining

A basic concept underlying the residual prediction is the liquid film over the screen openings. An assumption, which was deemed to be invalid for the S-IVC draining cases, is that the pressure drop across the top screen is negligible.

The "surface tension ΔP" is a significant parameter and represents a considerable head, particularly in LH_2 which has a relatively low density. It is also assumed that the gravity vector is pointing in the direction of the outflow.

Several approaches to screen wetting were taken in order to bracket the conditions ancitipated for actual operation. The standpipe screen wetting cases were:

1. screen is always dry
2. screen is initially wetted but once the film breaks it never re-wets

3. screen continuously re-wets if the film is broken, i.e. the surface tension ΔP is maintained across the screen although it is continuously being penetrated by vapor.

2.3.5 DRY SCREEN—Initially, $y = z = h$ (the problem is trivial up to this point). Decrease in volume V_z plus Q_{ab} is equal to the efflux Q_{ex}. Since the only ΔP available for flow is $\rho(y-z)$, $y > z$ during the entire outflow period.

2.3.6 INITIALLY WET SCREEN—At time zero $y = z = h$. Because the ΔP for flow Q_{ab} is

$$\Delta P = \rho \frac{g}{g_o} (y-z) + \Delta P\sigma$$

the necessary condition is $z > y$. If $y > z$ as in the dry case flow occurs from V_y into V_z. Because of this, for several seconds after $t = 0$, z remains constant at $z = h$ while y drops at the rate governed by $Q_{ab} = Q_{ex}$. Then because of decreasing flow ΔP due to decreasing head, Q_{ab} ceases to be as large as Q_{ex} and flow is required from the basket itself. At this point vapor is drawn into the basket through the screened openings to replace the liquid which is being discharged. If the screen does not re-wet, neglecting vapor flow losses across the standpipe, a strong reverse flow ($-Q_{ab}$) occurs to establish the level relationship for the dry screen case ($y > z$). The level relationships subsequently behave just as if the screen were always dry.

If the screen can continuously and instantly re-wet, continuously maintaining $\Delta P\sigma$, then the two fluid levels will remain at their relative positions, $z > y$, while they both approach zero. This is the limiting case opposite to the instantly drying screen of the previous case. These two solutions bracket the possible solutions.

The basic equations solved by the DREGS computer program are:

$$\frac{d}{dt}(V_y) = -Q_{ab}$$

$$\frac{d}{dt}(V_z) = Q_{ab} - Q_{ex}$$

Results of an analysis for the S-IVC LO_2 and LH_2 configurations, neglecting the top screen pressure losses, are presented in Reference 2. These results were shown to be invalid by the S-IVC scale model capillary device draining tests. An analysis considering top screen pressure losses was embodied in the DREGS2 program reported in Reference 19.

2.4 SETTLING ANALYSIS

In order to properly size surface tension devices for restart purposes it is necessary to know the time it takes to settle the propellants to various levels in the tank. Several investigators have attempted to solve this problem. Most notably, Masica and Petrash (Reference 20 ran a series of drop tower tests and correlated fluid velocities before impingement on the aft bulkhead based on the Bond number. Using the basic results of this study another drop tower correlation program was conducted at NASA LeRC to predict liquid accumulation rates in a Centaur scale model tank. This study by Salzman and Masica (Reference 21) gives geysering regimes as a function of Weber number. The equations given in this report have been arranged into a short computer program which will compute screen sizes to resist impingement forces, settling velocities, collection velocities and settling time. A listing of this program is given in Appendix A, Reference 1. Results of this program were compared with results of the MAC model for settling in the S-IVC LH_2 tank as discussed in Reference 1.

2.5 SURFACE TENSION PROPERTY VALUES

Low gravity phenomena and capillary device design are strongly influenced by the surface tension of the fluid being studied. Several investigators have experimentally determined the surface tension of cryogenics fluids which might be used in space applications or simulations. A survey of these experimenters was made to compile most of the available data for LH_2, LO_2, LF_2, LN_2 and LHe in order to determine differences between experimental values and to recommend values to be used for each fluid. The data is represented by the curves shown in the following figures with recommended values noted by an asterisk. The reader should bear in mind that surface tension vanishes at the critical temperature. The sources of data, indicated in the callouts on the graphs, are discussed in detail in Reference 1.

$$\sigma\left(\frac{LB}{FT}\right) = .686 \times 10^{-4} \times \sigma\left(\frac{DYNES}{CM}\right)$$

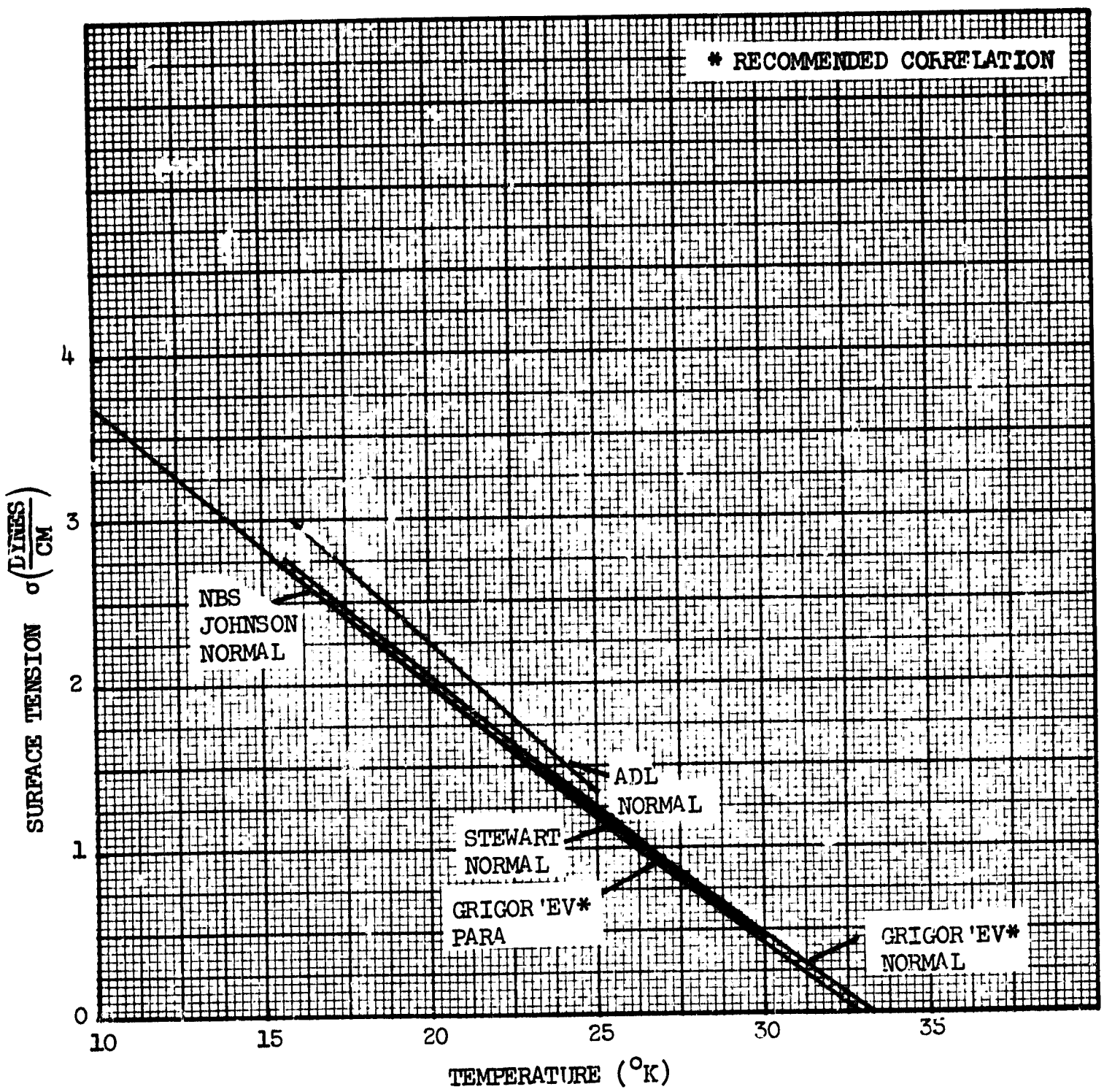


Figure 2-17. Surface Tension of Liquid Hydrogen

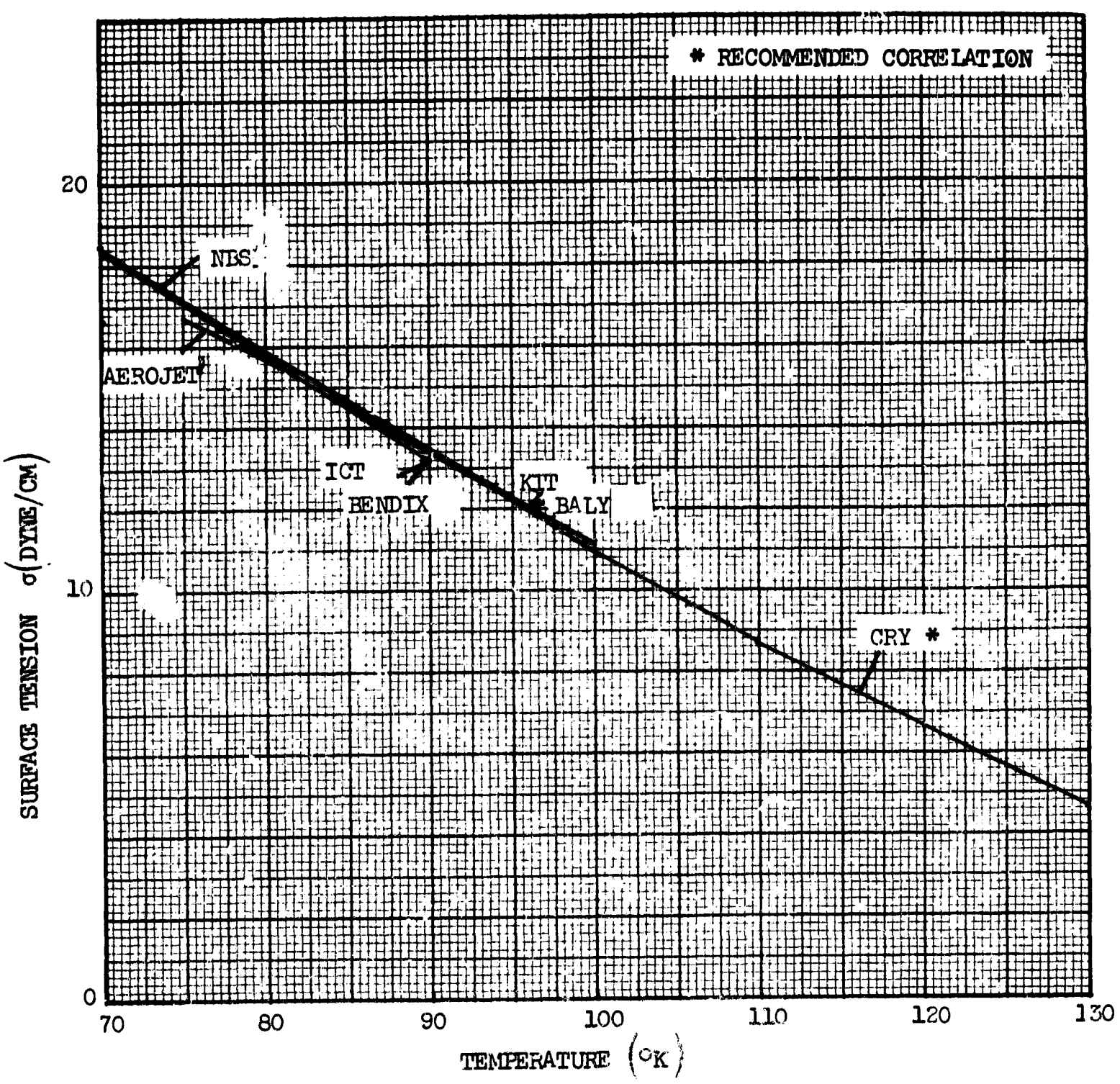


Figure 2-18. Surface Tension of Liquid Oxygen

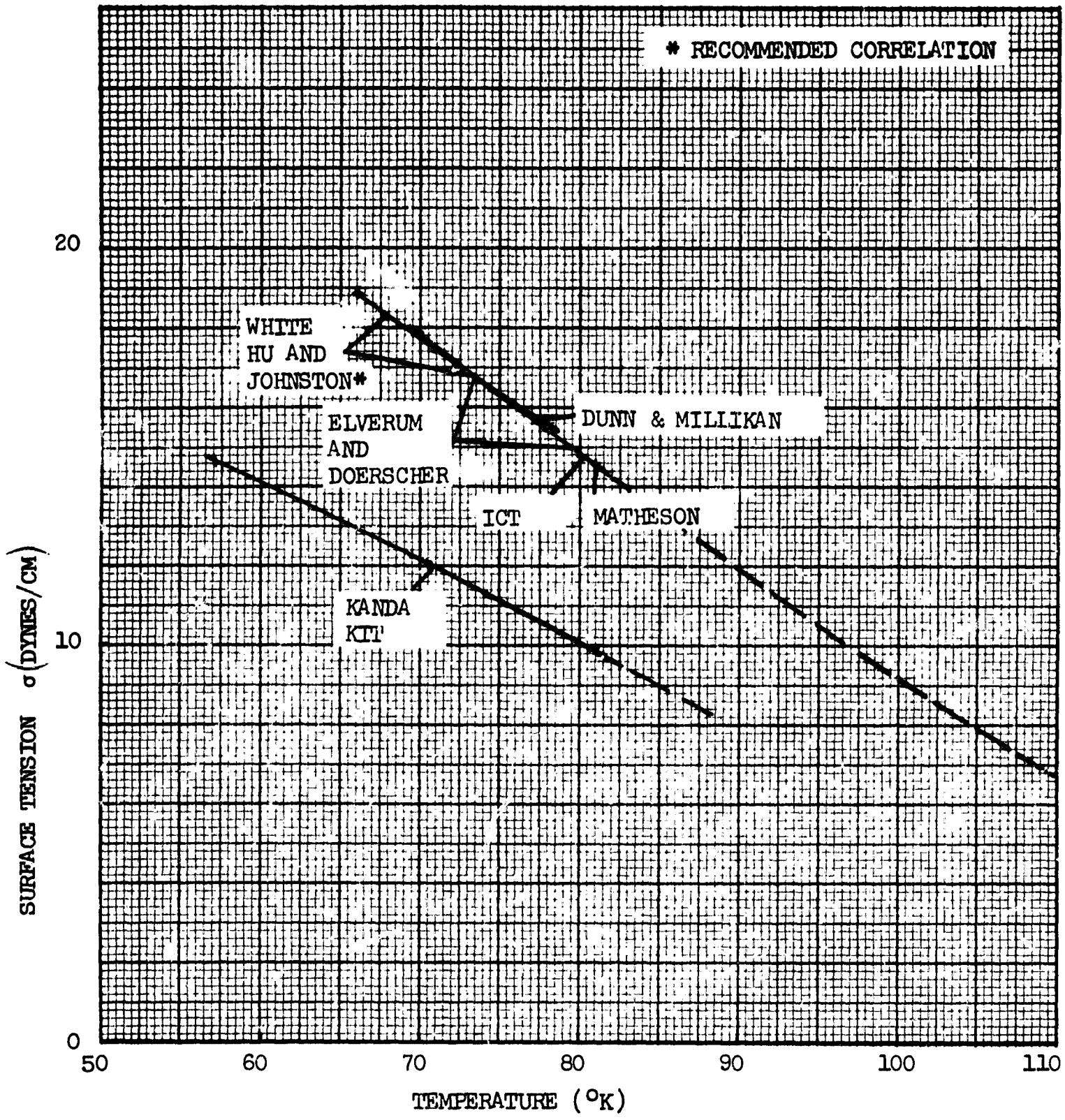


Figure 2-19. Surface Tension of Liquid Fluorine

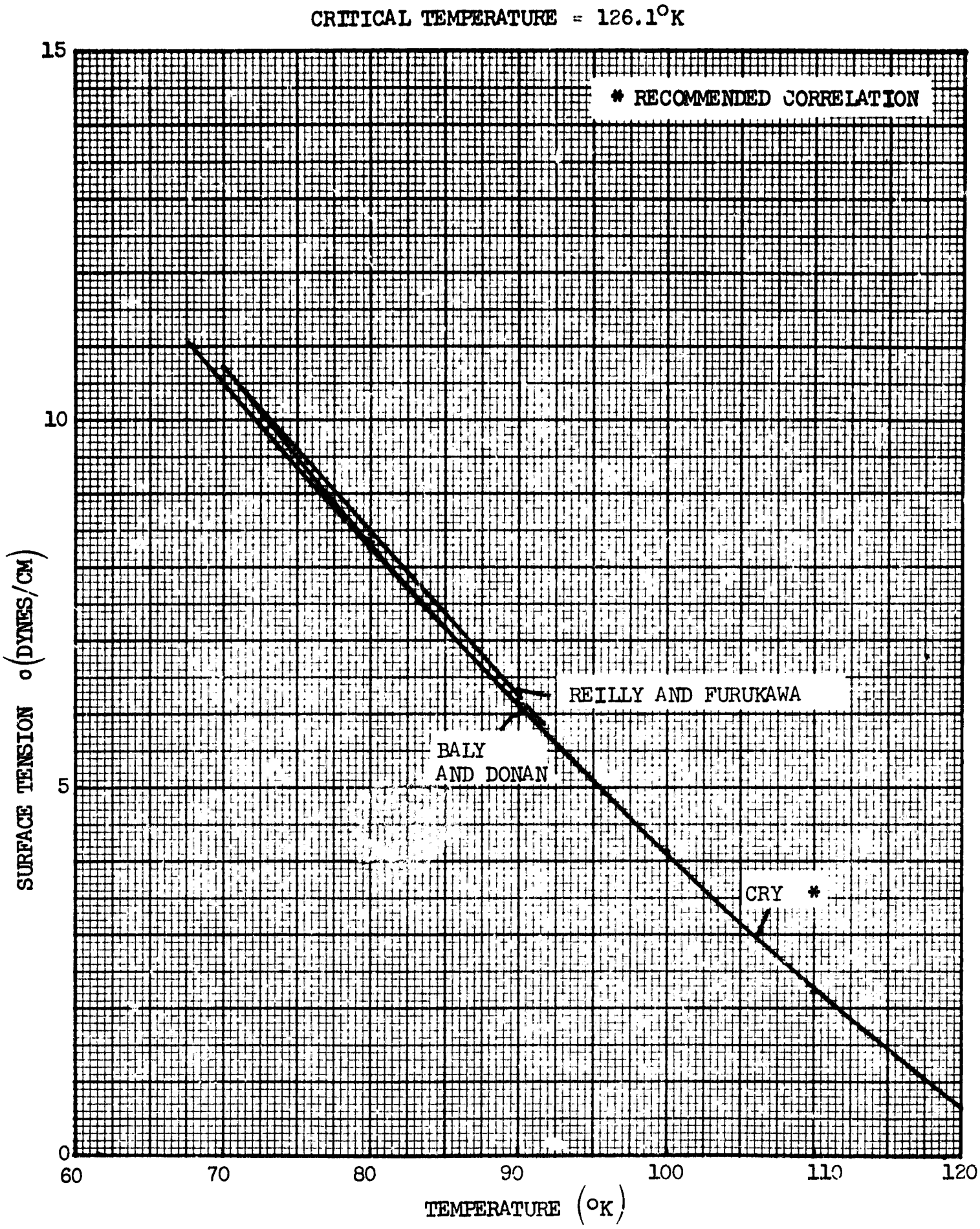


Figure 2-20. Surface Tension of Liquid Nitorgen

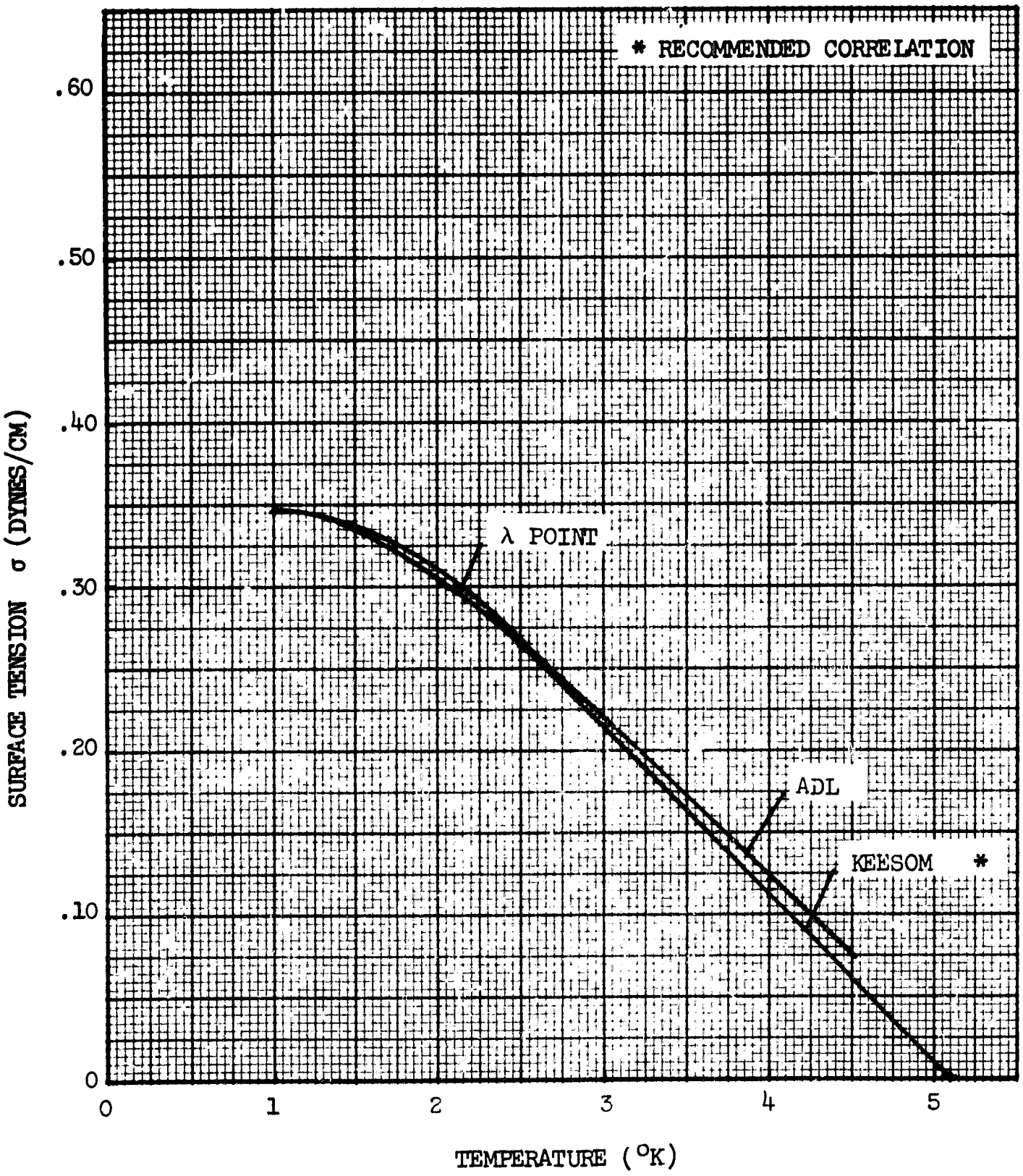


Figure 2-21. Surface Tension of Helium

3

REFERENCES

1. Bradshaw, R. D., Blatt, M. H., Burton, K. R., Evans, E. D. and Kneisel, K. M., "Thermodynamic and Fluid Mechanic Studies of Cryogenic Propellant," GDC-ERR-1332, December 1968.

2. Walburn, A. B., Blatt, M. H., Burton, K. R., and Leonhard, K. E., "Cryogenic Propellant Management," GDC-ERR-1420, December 1969.

3. Armour, J. C., and Cannon, J N., "Fluid Flow Through Woven Screens," AIChE Journal, Volume 14, Number 3, May 1968.

4. Washburn, E. W., "Note on a Method of Determining the Distribution of Pore Sizes in a Porous Material," Proceedings of the National Academy of Sciences, Volume 7, April 1921.

5. Morgan, P.G., "Fluid Flow Through Screens of Low Solidity," Journal of the Royal Aeronautical Society, Volume 66, 54, p 54.

6. Landau, L. D. and Lefshitz, E. M., Fluid Mechanics, Addison Wesley, 1959.

7. Aris, R., Vectors, Tensors and the Basic Equations of Fluid Mechanics, Prentice Hall, Inc., 1962.

8. Peebles, F. N., and Garber, J. H., "Studies on Motion of Gas Bubbles in Liquids," Chemical Engineering Progress, Volume 49, No. 2, February 1953.

9. Harmathy, T. Z., "Velocity of Large Drops and Bubbles in Media of Infinite or Restricted Extent," AIChE Journal, Vol. 6, No. 2, June 1960.

10. Swain, L. M., "On the Turbulent Wake Behind a Body of Revolution," Proceedings of the Royal Society of London, Series A, Vol. 125, p 647, 1929.

11. Schlichting, H., Boundary Layer Theory, McGraw-Hill, Inc., 1960.

12. Gibson, C. H., Chen, C. C., and Lin, S. C., "Measurements of Turbulent Velocity and Temperature Fluctuations in the Wake of a Sphere," AIAA Journal, Volume 6, No. 4, p 642, April 1968.

13. Saad, M. A., "Free Surface Behavior During Propellant Withdrawal," Joint AIAA/Aerospace Corporation Symposium on "Low Gravity Propulsion Orientation and Expulsion," Los Angeles, California, May 21-23, 1968.

14. Lubin, B. T., Springer, J. F. M., "The Formation of a Dip on the Surface of a Liquid Draining from a Tank," Journal of Fluid Mechanics, Volume 29 Part 2 pp 385-390, 1967.

15. Morgan, L., "Orbital Refueling and Checkout Study," Volume III, Part 2, LMSC T1-51-67-21. Contract NAS10-4606, 12 February 1968.

16. Lubin, B. T. and Hurwitz, L., "Vapor Pull Through at a Tank Drain with and Without Dulectraphorelic Baffling," Long Term Cryo-Propellant Storage in Space Conference, Huntsville, Alabama, October 1966.

17. Nussle, R. C., Derdul, J. D., and Petrash, D. A., "Photographic Study of Propellant Outflow from a Cylindrical Tank During Weightlessness," NASA TN-D-2572, January 1965.

18. Masica, W. J., Petrash, D. A., and Otto, E. W., "Hydrostatic Stability of the Liquid Vapor Interface in a Gravitational Field," NASA TND-2267, May 1964.

19. Blatt, M. H., Betts, W. S., Merino, F., Perkins, C. K., Siden, L. E., and Stark, J. N. "Low Gravity Propellant Control Using Capillary Devices in Large Scale Cryogenic Vehicles," Phase II Final Report, GDC-DDB70-008, Contract NAS8-21465, August, 1970.

20. Masica, W. J. and Petrash, D. A., "Motion of the Liquid-Vapor Interface in Response to Imposed Acceleration," NASA TND-3005, September, 1965.

21. Salzman, J. A., and Masica, W. J., "Experimental Investigation of Liquid Propellant Reorientation," NASA TND-3789, January 1967.